



ENERGY, ENVIRONMENT & STORAGE

AN INTERNATIONAL JOURNAL

Editor in Chief
Dr. Selahaddin Orhan AKANSU

Volume-2
Issue-3
September, 2022
ISSN:2791-6197

ENERGY, ENVIRONMENT AND STORAGE

EES JOURNAL

Founded and Published by Erciyes Energy Association



All rights reserved. It is forbidden to copy some or all of them with the written permission of the publisher.

Energy, Environment and Storage Journal is indexed in Crossref

Copyright © 2022

Printed in Turkey

ISSN-2791-6197

EES- EDITORIAL BOARD

HONORARY EDITORS:

Dr. T. Nejat VEZIROGLU

International Association for Hydrogen Energy, Miami, Florida, USA

Dr. Marc A. ROSEN

Faculty of Engineering and Applied Science, University of Ontario Institute of
Technology, Oshawa, Ontario, Canada

EDITOR IN CHEIF:

Dr. Selahaddin Orhan AKANSU

Erciyes University

Engineering Faculty

Mechanical Engineering Department

38280, Kayseri, Turkey

ASSOCIATE EDITOR IN CHIEF:

Dr. Nuray ATES

Erciyes University

Engineering Faculty

Environmental Engineering Department

38280, Kayseri, Turkey

BOARD MEMBER

Dr. Abdul Hai Al Alami

University of Sharjah, Department of Sustainable and Renewable Energy Engineering, Sharjah, UAE

Dr. Richard Gilles Agbokpanzo

University of Abomey, Department of Industrial Science and Techniques, Higher Normal School of Technical Education, Benin, West Africa

Dr. Abdülaziz Mohamed Atabani

Erciyes University, Department of Mechanical Engineering, Kayseri, Turkey

Dr. Sehnaz Sule Kaplan Bekaroğlu

Süleyman Demirel University, Department of Environmental Engineering, Isparta, Turkey

Dr. Michela Costa

Istituto Motori (CNR), National Research Council of Italy, Naples, Italy

Dr. Filiz Dadaşer Çelik

Erciyes University, Department of Environmental Engineering, Kayseri, Turkey

Dr. Bilge Albayrak Çeper

Erciyes University, Faculty of Aeronautics and Astronautics, Kayseri, Turkey

Dr. Sabri Deniz

Lucerne University of Applied Sciences and Arts, Institute of Mechanical Engineering And Energy Technology Ime, Luzern, Switzerland

Dr. Slawomir Dykas

Silesian University of Technology, Department of Power Engineering and Turbomachinery, Gliwice, Poland

Dr. Gamze Genç

Erciyes University Department of Energy Systems Engineering, Kayseri, Turkey

Dr. Hikmat S. Hilal

An-Najah National University, Inorganic & Materials Chemistry, Nablus, West Bank, Palestine

Dr. Nafiz Kahraman

Erciyes University, Faculty of Aeronautics and Astronautics, Kayseri, Turkey

Dr. Amer Kanan

Department of Earth and Environmental Sciences, Al-Quds University, Jerusalem, Palestine

Dr. Shpetim Lajqi

University of Prishtina “Hasan Prishtina”, Faculty of Mechanical Engineering, Prishtina, Kosovo

Dr. Hamid Mukhtar

Institute of Industrial Biotechnology, Government College University, Lahore, Pakistan

Dr. Tuğrul Oktay

Erciyes University, Faculty of Aeronautics and Astronautics, Kayseri, Turkey

Dr. Farooq Sher

Coventry University, Aerospace and Automotive Engineering, Faculty of Engineering, Environment and Computing, United Kingdom

Dr. Ghulam Hasnain Tariq

Department of Physics, Khawaja Fareed University of Engineering & Information Technology, Rahim Yar Khan, Pakistan

Dr. Sezai Alper Tekin

Erciyes University, Industrial Design Engineering, Kayseri, Turkey

Dr. Sebahattin Ünal

Erciyes University, Department of Mechanical Engineering, Kayseri, Turkey

EDITORIAL OFFICE

Caner ŐİMŐEK

Süleyman OSMANLI

Esenay ARSLAN

Enes FİL

AIM AND SCOPE

Energy, Environment and Storage papers consider the prospects of energy technologies, environment, materials, process control and industrial systems. The Energy, Environment and Storage will be published 3 times per year.

Contributions describe novel and significant applications to the fields of:

- Hydrogen Fuels
- Hydrogen and Fuel Cell
- Hydrogen Economic
- Biomass
- Solar PV Technology
- Solar Thermal Applications
- Wind Energy
- Materials for Energy
- Drones and Energy Applications
- Nuclear Energy and Applications
- Hydro Power
- Fuel Technologies (CNG, LNG, LPG, Diesel, Gasoline, Ethanol, etc.)
- Numerical Modelling
- Energy Storage and Systems
- Battery Technologies
- Energy Management
- Heat and Mass Transfer
- Aerodynamics
- Aerospace and Energy Applications
- Combustion
- Electric Vehicle Transportation
- Off-grid Energy Systems
- Environment Management
- Air Pollution
- Water and Wastewater Pollution
- Water and Wastewater Management
- Waste Management
- Global Warming and Climate Change
- Environmental Ecosystem
- Environmental System Modelling and Optimization
- Ecological Applications or Conservation

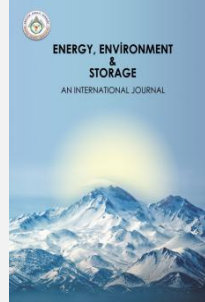
CONTENTS

<i>Carbon Black Production from Various Sources by Thermal Cracking Method</i> (Research Article)	1
Achal Pandey, Srinivasarao Naik B, Shishir Sinha, B. Prasad	
<i>Testing of Ethylene Glycol Ketal, Dioxane and Cyclopentanone as Components of B10, B20 Fuel Blends</i> (Research Article)	9
Ibrahim Mamedov, Gular Mamedova, Nargiz Azimova	
<i>Investigation of the Performance Changes of the Savonius Wind Turbine Rotors with the Same Front View Area of Look by Change of the Aspect Ratio</i> (Research Article)	13
Mahmut Burak Akkus, Zeki Hakseve, Süleyman Osmanlı	
<i>Phase Change Materials for Energy Efficiency in Building Components – Overview</i> (Review Article)	23
Rachit Agarwal, Pradeep Rawat, Devendra Rai, Humaira Athar, Srinivasarao Naik B	
<i>Hydroelectric Power Overview in 2021 of Turkey</i> (Research Article)	30
Alaeddin BOBAT	



Energy, Environment and Storage

JournalHomepage: www.enenstrg.com



Carbon Black Production from Various Sources by Thermal Cracking Method

Achal Pandey^a, Srinivasarao Naik B^{ac}, Shishir Sinha^{ab}, B. Prasad^a

^a Chemical Engineering Department, Indian Institute of Technology Roorkee, Roorkee-247667, Uttarakhand

^b Central Institute of Petrochemicals Engineering & Technology, Chennai-600032, Tamil Nadu

^c Innovative Building Materials Group, CSIR-Central Building Research Institute, Roorkee-247667, Uttarakhand

ABSTRACT: Petroleum-based feedstock (PBFS) and Coaltar-based feedstock (CTBFS) were used for the synthesis of carbon black (CB) via thermal cracking method named as Petroleum-based feedstock carbon black (PBFS-CB) and Coal tar-based feedstock carbon black (CTBFS-CB) in a furnace reactor at a temperature of 1800 °C, for utilizing industrial waste products. The obtained distinguish carbon black samples are characterized for determining functional groups, morphology, and surface area using advanced instruments. Further, investigated physical and mechanical properties of obtained different CB samples mixed into the natural rubber. The small clusters morphology is observed in CBs. There are slight changes in spectra peaks and there no significant new peaks are observed. The same minerals observed at same theta values in XRD pattern corresponding to PBFS-CB and CTBFS-CB. The tensile strength, modulus 300% and abrasion loss of samples into rubber were determined as per international ASTM standards. The results revealed that, there are negotiable values observed in both samples due to minimal changes observed in surface area of the CB samples. These samples can be used for various applications viz rubber reinforcement, conductivity agent, colouring agent, and ultraviolet screening agent etc.

Keywords: Carbon black, thermal cracking, Petroleum-based feed stock, Coal-based feedstock, ASTM -CB standard

Doi: <https://doi.org/10.52924/NSVQ3567>

1. INTRODUCTION

Carbon blacks (CBs) are produced by partial combustion or thermal cracking of hydrocarbons such as petroleum-based feedstocks, coal tar-based feedstocks and spent tyre oil etc. under delimited conditions (Okoye et al., 2021). Approximately 90% to 95% of CBs are produced globally in furnaces using renewable and non-renewable feedstocks. Aromatic oil is produced as a by-product of natural gas and acetylene manufacturing (Cheng et al., 2020). The cost of feedstock accounts for roughly 60% of the entire cost of CB manufacture. Carbon particles are produced in a variety of ways such as AC thermal plasma, vapor thermolysis, pyrolysis, hydrolysis and carbonization (ICBA, 2016). CB is made up of more than 90% of untainted carbon in total composition and generally spherical carbon atoms of colloidal size that fuse together in aggregates (Ciobanu et al., 2016). CBs are produced in agglomerates form by above mentioned methods, which disintegrate during the rubber-stirring procedure (Ikram and Hashin, 2002). In ordinary parameters, the tiniest dispersible unit in the rubber matrix is the tiny cluster. Hence, clusters are frequently perceived as the emphasizing items themselves (Shah et al., 2013). This carbon black is used

Corresponding author: shishir@ch.iitr.ac.in

as an agent such as thermal conductivity agent, colouring agent, an infrared airing agent and extensively used in printing as coatings, inks, plastics and others (Donnet et al., 2018). Particularly, 89.5% of CB goes into rubber industries, for production of tires (Wang and Yan, 2011). The physical qualities such as tear strength and tensile strength can be improved by incorporation of carbon black in rubber. CB improves viscidness and the rigidity of rubber and is one of most excellent filler substances commercially available in the market (Chandrasekaran, 2010). CBs are manufactured commercially using a variety of technologies. These are available in the form of various black names such as furnace, lamp, thermal, acetylene and channel black, which were given names based on according their manufacturing procedures (Kato et al., 2018). Thermal black and channel black come in a variety of grades, including N880 and N990, and are utilized in a variety of rubber compounds. Acetylene blacks (ABs) and lamp blacks (LBs) were developed by the Chinese for use synthetic substances and black ink. AB is a thermal conductive agent using in rubber substances (Bansal et al., 1993). The CB cluster morphology, surface functional groups and particle size distribution of CBs can be tailored during manufacturing methods (IEA, 2007). The particle

size in micro/nanometres increases outside or exterior surface area and develops crystalline dendritic structure, enhances the reinforcing performance in rubber. The reinforcing performance is generally better when particle size distribution is below micro/nanosize (Wang et al., 2003). For large-scale production, selectivity in carbon black qualities has been developed by controlling temperature, residence time, and feedstock-to-air ratio, in certain cases with the addition of coagulation suppressor (Mark et al., 2005). Due to serious environmental consequences such as global warming and crisis in climate, international societies are gradually challenging rubber industries for utilization of renewable resources for carbon black production (Park and Kim, 2000). Therefore, CB production derived from alternative feedstocks such as renewable resources and recycling of waste materials. The industrial process, production techniques and composition of renewable feedstock are impacts on the yield, physical characteristics, and chemical properties of CBs (Quan et al., 2018). CB has excellent thermal stability in inert environments, as well as mechanical and electrical conductivity. It is a biocompatible substance that is chemically stable in non-oxidizing environments (Snowdon et al., 2014). Year-over-year rise in global demand for new automobiles has resulted in an increase in tyre manufacturing and tyres destined for waste. The rubber tyre's service life is finite, and is possible to re-treat them to extend their life (Rodgers, 2015). A few research articles related to the manufacturing of CBs from various petroleum feedstocks are briefly discussed. Rubel (1970) prepared amorphous form of carbon black from petroleum oil for automotive tires using combustion method. Kaminsky et al. (2019) used synthetic and natural rubber as a feedstock for production of aromatic oil and carbon black. The pyrolysis temperature, fluidizing gas type, and gas residence duration in the pyrolysis reactor were all tuned during main products. Pyrolysis tars, clarified oils, aromatic extracts, and vacuum residue were examined by Srivastava et al. (1990) Pyrolysis tar is one of the feedstocks that can be used to make carbon black. The aromatic extract comes next. Roy et al. (1994) prepared oil and carbon black under vacuum pyrolysis method using tyres as feedstocks. Zhou et al. (2018) used leftover tea to make carbon black by physically activating it with steam. The effects of activated carbon yield and pore properties on activation temperature were examined. Due to the breakdown of cellulose and hemicellulose, the yield dropped as the activation temperature was raised. The BET method, temperature plot method and Langmuir equation were exploited to calculate volume of pore and surface area of CB. As activation temperature rose, more volatile components were released, increasing the specific surface area and micro-pore volume. According to Khalil et al. (2010), CBs were made from organic substances such as Coconut shells (CNS), Bamboo stem (BS), and oil palm (OP). These organic substances were by pyrolysis at 700 °C. The synthesised CB had porosities that are well-developed and was primarily composed of micro-pores. Lee et al. (2017) exploited thermal treatment with CB in order to make a petroleum-based

binder pitch to enhance percentage of coking yield and tensile strength of carbon discs.

The goal of this research is to produce CBs from petroleum-based feedstock (PBFS) and coal tar-based feedstock (CTBFS) by thermal cracking method. The impact of feedstock type on Chemical Properties of carbon black and Mechanical Properties of Rubber compound (Natural Rubber Filled with carbon black) are examined. It would be interesting to know how changes in feedstock affect the vulcanizate's physical properties.

2. RAW MATERIALS AND PREPARATION METHOD

2.1 Raw Materials

Petroleum-based feedstock (PBFS) taken from Reliance Industries Limited, Jamnagar, Gujrat, India and Coal tar-based feedstock (CTBFS) taken from Epsilon Carbon, Karnataka, India. These two feedstocks were used for the production of CBs. natural rubber (ISNR 3 CV), zinc oxide (ZnO), stearic acid, carbon black, and MBTS were used for rubber formulations. The characteristics of PBFS and CTBFS feedstocks are provided in Table 1.

Table 1 Characteristics of different Feedstocks

Characteristics	Test Method	Value	
		PBFS	CTBFS
Specific Gravity @15.56°C (gm/cc)	ASTM D 1298	1.08	1.14
API Gravity	ASTM D 1298	0.99	-7.3
Viscosity@ 98.9°C (SUS)	ASTM D 88	89	56
BMCI	Phillips 7317	126	167
Sulphur Content (%)	ASTM D 7679	0.80	0.49
Water Content (%)	ASTM D 95	0.2	0.5

*PBFS: Petroleum based feedstock; CTBFS: Coal tar-based feedstock; API Gravity: American Petroleum Institute gravity, is a measure of how heavy or light a petroleum liquid is compared to water; BMCI: Bureau of Mines Co-relation Index, effectively measures the degree yield of Carbon Black

The viscosity of these two feedstocks performed using Saybolt viscosity bath for Automatic viscosity timing (Make: Koehler instruments company, inc. USA and Model: SV4000) at different temperature for determining the flow properties for atomization in furnace reactor. It is key parameter for weather feedstocks can easily inject in reactor or not. As temperature is increased, the flow properties of PBFS and CTBFS are improved as shown in Fig.1. It means these two feedstocks easily atomize in furnace reactor. The rheometer, Moving Die Rheometer C (Make Alpha Technologies Hudson Ohio, USA), a convenient instrument was used to evaluate the effects of carbon black rubber interactions on rate of cure, was employed for the purpose of characterizing critical parameters

related to the vulcanization process. The rheological parameters are provided in Table 2

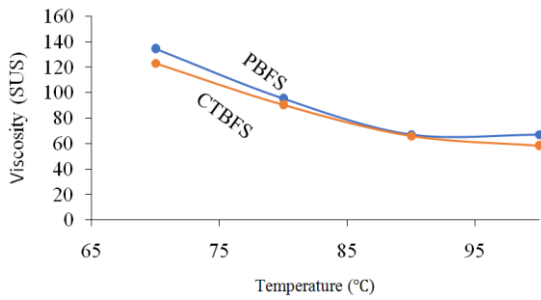


Fig.1 Viscosity in SUS of different feedstocks at various temperature

*SUS: Saybolt Universal Seconds

Table 2: Rheometric data of different CBs

Parameters	PBFS-CB	CTBFS-CB
ML(lbf-in)	3.06	3.43
MH (lbf-in)	15.88	16.52
TC90 (mm: mm)	20.70	19.33
TS2 (mm: mm)	2.71	2.51
MH-ML (ΔM) (lbf-in)	12.82	13.09

*ML: Minimum torque is a measure of the extent of mastication; MH: Maximum torque is an indication of the cross-linking density of the fully vulcanized rubber; TC90: the time required for the torque to reach 90% of the maximum; TS2: the time from start of the test to the moment when the torque value increases for 2 lbf-in above the ML value; MH-ML(ΔM): range of torque change

2.2 Preparation Of Different Cbs From Different Sources

The Petroleum-based feedstock was preheated at temperature of 210 °C and it injects into furnace reactor through a fine orifice nozzle to atomizer PBFS and in simultaneously of preheated atmospheric air blowing at the temperature 750 °C to facilitate the combustion of PBFS. The ample amount of heat is being liberated due to exothermic nature of reaction and raising the furnace reactor inside temperature up to 1800 °C. At this high temperature, the thermal cracking of hydrocarbons in PBFS occurs and produces carbon black along with high calorific value flue gases (CB-HCVFG). The produced CB-HCVFG used as a source of heat, is recirculating in counter flow direction of PBFS and atmospheric air to increase the initial temperature of inlet PBFS and atmospheric air through heat exchange equipment’s, known as Oil pre heater (OPH) & Air pre heater (APH) respectively. In this continuous process, thermal cracking of PBFS in furnace reactor is slowing down by sprinkling of water at the end of furnace reactor to obstruct complete combustion of PBFS and to facilitate of carbon black generation. After recovery of heat from

CB-HCVFG via preheating the inlet PBFS and atmospheric air, the CB-HCVFG passes through filtration process to separate the carbon black (CB) from HCVFG (Fig.1). The obtained carbon black is characterizing with help of sophisticated further processes, i.e., binder addition, palletization, drying etc. The same procedures were repeated with CTBFS to produce another type of carbon black.

2.2.1 Preparation of Rubber with Different Cbs

The obtained CBs samples were dried at 125 °C for 1 hour and cooled till ambient temperature was reached. Until ready to mix, stored the CBs in an airtight, moisture-proof container. Natural rubber (ISNR 3 CV), zinc oxide (ZnO), stearic acid, carbon black, and MBTS were fed into an open mill machine after heating at 70 °C and set the mill opening at 1.4 mm to start the mixing in sequence of ASTM D 3192. The obtained rubber sheet is conditioned at 23 °C for one hours before bringing the mould to the curing temperature in closed press. Placed 70 gm of rubber compound in the mould cavity and vulcanised for 30 minutes at 145 °C and 135 MPa pressure for the fabrication of rubber sheets (Farida et al., 2019). The raw material composition in parts per 100 parts of rubber (PHR) has been carried out as per ASTM D 3192 (Table 3).

Table 3 Preparation of rubber compound with different CBs

Ingredients for rubber sheet	PBFS (PHR)	CTBFS (PHR)
Natural Rubber (ISNR 3 CV)	100.0	100.0
Carbon Black	50.0	50.0
ZnO	5.0	5.0
Stearic Acid	3.0	3.0
MBTS	0.60	0.60
Sulphur	2.5	2.5

*PHR: Parts per 100 parts of Rubber(weight of ingredients are in gram w.r.t. 100 gram of rubber)

2.3 Characterization of CB samples

2.3.1 Morphology of CB samples

The collected CBs were taped to the sample holder with carbon tape. A gold sputter coater was used to coat the CBs for conductivity. The samples were placed in FESEM (Make: TESCAN, Model: MIRA 3).Examined the morphology of various CBs at 20 kV.

2.3.2 Fourier Transform Infrared spectroscopy (FTIR)

The CBs were mixed with KBr. Prepared CBs sample pellet using pelletizer. The prepared pellet was placed in FTIR (Make: PerkinElmer, Model: spectrum 2). Operated FTIR from 450 to 4000 cm-1and examined functional groups contained in various CBs.

2.3.3 X-ray diffraction of CB samples

The CBs were powdered, and the powdered samples were poured onto a glass slide. After flattening the powdered samples with the help of spatula, the glass

slide was placed in X-ray diffraction (Make: Rigaku Model: DMAX2200). The XRD operated at a rate of 3 theta/min within the functioning range 2θ : 0-70. (Srinivasaraonik et al., (2021). Investigated the mineralogical properties of CBs samples with existing d-values in the system. Figure 2 gives preparation of carbon black flow diagram.

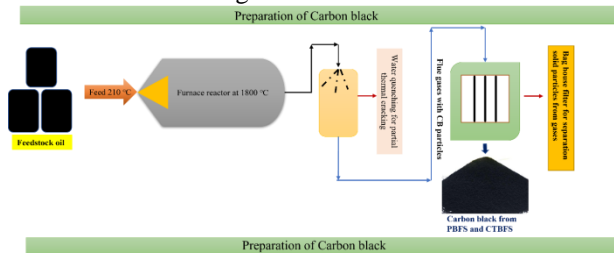


Fig.2 Flow diagram for preparation of various carbon black

2.3.4 Particle size distribution of CB samples

The CB samples were dispersed in Isopropanol as solvent. The dispersed samples were taken into Particle Size Analyzer (Make: Horiba, Model: LA-950). The particle size distribution curve of various CBs was observed at refractive index of 0.5.

2.3.5 BET analysis of CB samples

BET method was used as per the ASTM D6556. The surface area is determined by N_2 adsorption and desorption at 77K and partial pressure (Lippens and Boer, 1965). The BET Equation is used to calculate the filler's surface area:

$$S_{BET} = V_m \times N \times a_m \times 10^{-18}$$

Here, V_m is Monolayer adsorbed volume; N is Avogadro constant (6.02×10^{23} 1/mol), a_m is 0.16 i.e., N_2 molecular surface area.

2.3.6 Colloidal Properties of different CB samples

Oil absorption number, Iodine adsorption number, and compressed oil absorption number were determined according to ASTM D 2414, ASTM D 1510, and ASTM D3493.

2.3.7 Proximate analysis of CBs

Proximate analysis is widely used to determine moisture, volatile matter (VM), fixed carbon (FC) and ash content of CBs. The proximate analysis was done as per ASTM D 162-84 method

2.3.8 Determination of tensile strength

Conditioned the cure rubber sheet for an hour at room temperature and cut the dumbbell from it. Determined the thickness of the thin portion of dumbbell and marked it. Set the tensile tester machine parameter for Test speed and Gauge length at 500 mm/min and 25 mm respectively. The tensile strength and modulus 300 percent of CBs in rubber were evaluated using a Tensile Testing Machine -Zwick 1435 (ZwickRoell Pvt. Limited Germany) in accordance with ASTM D412.

2.3.9 Dynamic properties of CB samples in rubber

ASTM D5963 and ASTM D 623 methods were used to investigate the dynamic parameters of CB samples into the rubber, i.e., abrasion loss and heat buildup (HBU). The rubber sheet was cured at 145 °C for 30 mins. The abrasion loss of rubber sheets was measured at vertical force load 10N. As well as heat buildup of rubber sheet was measured for 30 minutes at set temperature 100 °C conditioned for 30 minutes.

2.3.10 Rheological properties of CB samples in rubber

Moving Die Rheometer C (Make: Alpha Technologies Hudson Ohio, USA) used for determination of rheological properties of CBs in rubber. It is an expedient instrument was used to evaluate the effects of carbon black rubber interactions on rate of cure of rubber. It was employed for characterizing critical parameters of CBs in rubber which is related to the vulcanization process.

3. RESULTS AND DISCUSSIONS

3.1 Morphology of CBs

The morphology of various samples PBFS-CB and CTBFS-CB are from PBFS and CTBFS shown in Fig.3. The majority of CB particles form a cluster aggregate, while an insignificant percentage of CBs aggregate closer together to form a bigger CB block (Fig.3 (a) and (b)).

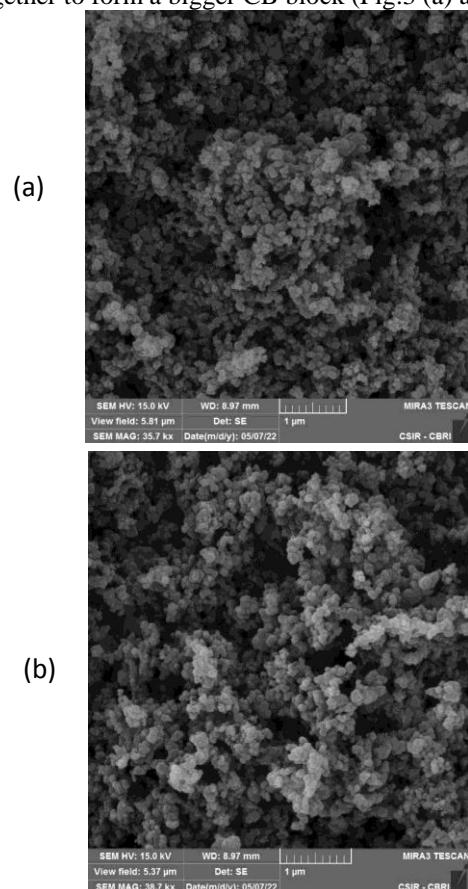


Fig.3 Morphology of different carbon black (a) PBFS-CB (b) CTBFS-CB

These CB micro particles, on the other hand, are approximately ring-shaped and are practically linearly connected. The aggregate's total size is slightly lower. It has a more developed spatial structure and is improving, implying that the reinforcing performance will improve.

3.2 X-ray diffraction analysis of CBs

Fig.4 shows the XRD analysis of various CBs generated at 1800 °C. Both diffractograms exhibit two broad peaks, showing that the two samples are amorphous carbon materials with limited crystallinity areas Fig. 4(a) and (b). The planes of graphitic structures are represented by the peaks at 25.9° in both samples, and the graphitic structure planes are represented by the second intensity peak at about 44.7° in the samples. Both of these peaks confirm that the CBs were successfully transformed into

graphitic nanostructures at high temperatures. Furthermore, there is no significant a prominent peak observed. Due to impurities, the XRD patterns indicate that the purity of the CBs produced in this experiment is higher, which is consistent with the results given in Fig. 4 (a) and (b).

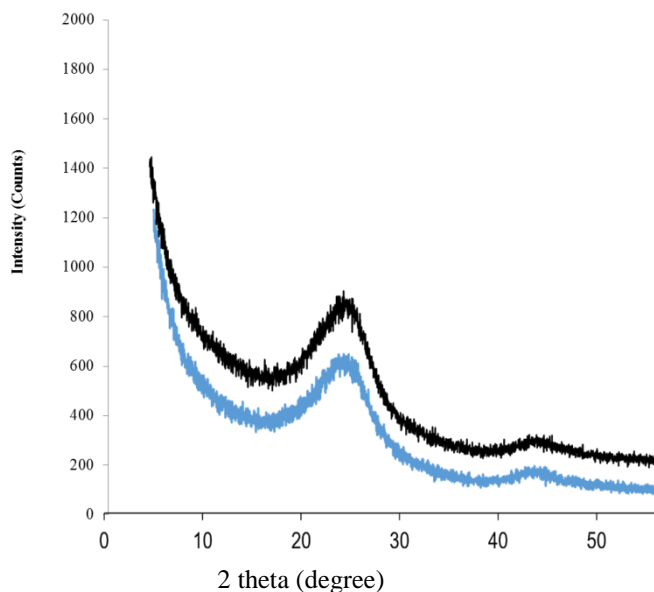


Fig.4 XRD analysis of different carbon black samples (a) PBFS-CB (b) CTBFS-CB

3.3 FTIR analysis of CBs

FTIR analysis of various CBs functional groups are shown in Fig. 5. Nonbonded hydrogen group, OH stretching, Methane (=CH-) C-H stretching, and Methylene (=CH₂) C-H stretching were identified in the spectra of PBFS-CB peaks 3595 cm⁻¹ and 2875 cm⁻¹, respectively. Alkenyl C=C stretching and Skeletal C-C stretching have absorption maxima of 2085-1489 cm⁻¹. Stretching vibrations peaks at 965-854 cm⁻¹ and 694 cm⁻¹ are observed corresponding to trans C-H out-of-plane bend and cis C-H out-of-plane bend in Fig. 5(a). The FTIR analysis of CB functional groups of CTBFS-CB has shown in Fig.5 (b). Nonbonded hydrogen group, OH stretching, Methane (=CH-) C-H stretching, and Methylene (=CH₂) C-H stretching were identified in the spectra of CTBFS-CB peaks 3597 cm⁻¹ and 2870 cm⁻¹, respectively. The absorption maxima for Alkenyl C=C stretching and Skeletal C-C stretching are 2089-1493 cm⁻¹ and 2089-1493 cm⁻¹, respectively. Stretching vibrations of the functional groups such as trans C-H out-of-plane bend and cis C-H out-of-plane bend are seen at 962-859 cm⁻¹ and 697 cm⁻¹, respectively (Fig. 5(b)).

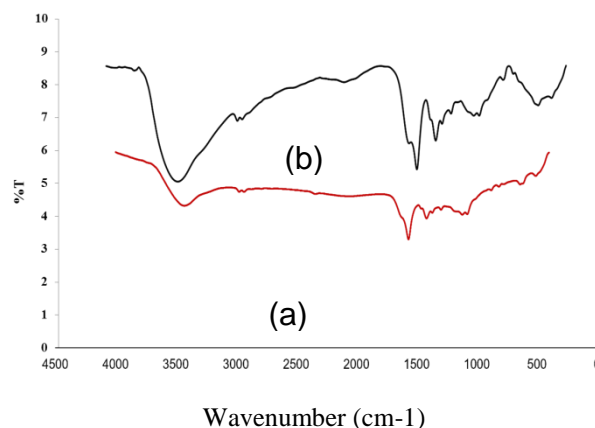


Fig.5 FTIR analysis of different carbon black samples (a) PBFS-CB (b) CTBFS-CB

The PBFS-CB and CTBFS-CB products obtained from the furnace reactor at 1800 °C revealed there is no significant differences observed. In both cases, changes in carbon percent had little effect on the spectra peaks, as seen in Table 4 (Wibawa et al., 2020).

Table 4 Proximate Analysis of different carbon black samples

Parameters	Test Method	PBFS-CB	CTBFS-CB
Moisture	ASTM D 1509	1.6	1.5
Ash	ASTM D 1506	0.18	0.26
Volatile	ASTM D 1620	4.6	4.7
Fixed carbon	ASTM D 7679	93.02	91.2

*PBFS-CB: Petroleum based feedstock carbon black; CTBFS-CB: Coal tar-based feedstock carbon black
Note – ASTM D 1620 “Method of test for volatile content of carbon black” was discarded in 1972

3.4 Particle size distribution of CBs

The particle size analysis of the various CBs is displayed in PSA with a poly-dispersion index of 0.5, and their pattern is shown in Fig. 6. The statistical computation of the created curve pattern of the particles size distribution of the CBs material is shown in this figure. A mean diameter of 1305 nm (1.3 μm) (PBFS-CB) and 1360 nm (1.36 μm) (CTBFS-CB) with a standard deviation (SD) of 1245 nm (1.24 μm) (PBFS-CB) and 1246 nm (1.24 μm) (CTBFS-CB) can be noticed, with a standard deviation (SD) of 1245 nm (1.24 μm) (CTBFS-CB). Various CBs modes are 548 nm (0.54 μm) and 624 nm (0.62 μm), which correspond to PBFS-CB and CTBFS-CB, respectively. CB particle populations in PBFS-CB range from 907 nm (0.9 μm) to 1305 nm, while CB particle sizes in CTBFS-CB range from 966 nm (0.9 μm) to 1361 nm (1.36 μm) (Fig.6). The poly dispersion (PI) index of CBs is 0.5, which explains the undersize proportion. However, the smaller the particles, the better the surface area characteristics, and the produced CBs were then studied further.

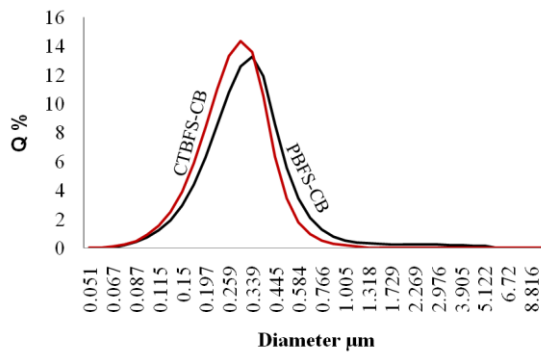


Fig. 6 Particle size distribution of different samples (a) PBFS-CB (b) CTBFS-CB

3.5 Surface area of various CBs

BET surface area of CBs manufactured at 1800°C utilizing the same procedures from various sources, namely PBFS and CTBFS. The surface area of several CBs was determined using BET. Because it indicates the extent of the interface, such as the availability of the surface for crosslinking between rubber chains and carbon black, surface area is an important morphological parameter for carbon black reinforcing capability. The surface area result could help determine not only how much of the area that rubber can absorb into the carbon black, but also how much of the area that rubber can absorb into the carbon black. CBs produced from PBFS and CTBFS had surface areas of 112.6 m²/g and 111.06 m²/g, respectively (Fig.7). PBFS-CB and CTBFS-CB have not changed much as a result of nuclei at high temperatures enlarging due to the adhesion of intermediate products. Due to uneven adherence in both cases, additional micro-pores generated throughout the adhesion process, resulting in a nearly constant BET surface area. The BET surface area constant of the thermal degradation process at 1800 °C was likewise consistent with XRD analyses (Fig.4).

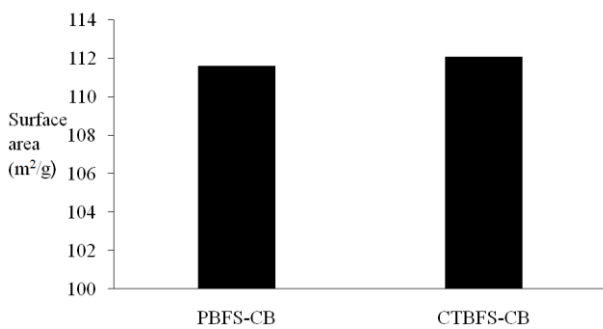


Fig.7 Surface area of various carbon black samples

3.6 Proximate analysis of CBs

The proximate analysis of PBFS-CB and CTBFS-CB are given in Table 4. The mass fraction of moisture content and volatile matter are same observed in both samples. The ash and fixed carbon are 0.18 wt.% and 93.02 wt.%, 0.26 wt.% and 91.2 wt.% corresponding to PBFS-CB and CTBFS-CB respectively. The ash content and fixed carbon differed due to slightly change in volatile matter (Table 4.).

3.7 Colloidal properties of various CBs incorporated the natural rubber

The colloidal characteristics of different CBs were determined using ASTM D 2414, ASTM D 1510, and ASTM D 3493, which stand for Oil absorption number,

Iodine adsorption number, and compressed oil absorption number, respectively. Table 5 shows their respective values. The results of the iodine adsorption method have been confirmed to be favourably linked with the BET method. CB is first mixed in an iodine solution. The excessive amount of iodine is titrated using a normal sodium thiosulfate solution. The carbon black surface area determines the eventual adsorption number (AN). The iodine adsorption values of PBFS-CB and CTBFS-CB are 121.5 mg/g and 120.8 mg/g, respectively. Moisture absorbed, Pores, volatiles, and sometimes ageing can affect the surface area of the filler (Mark et al., 2013). Furthermore, the DBP absorption of these CBs is 114.2 and 113.6 cc/100 gm for PBFS-CB and CTBFS-CB, respectively. These are high values (Table 5), showing that the quantity of assemblages formed by these CB nanoparticles is bigger and that a large number of void spaces are developed, implying that the aggregate's spatial arrangement is better overall.

Table 5 Colloidal Properties of different carbon black samples

Parameters	Test Method	PBFS-CB	CTBFS-CB
Fines (%)	ASTM D 1508	4.6	5.2
Sieve residue (#35) (%)	ASTM D 1514	0.0005	0.0001
Pellet hardness (25%) (Gf)	ASTM D 3493	24.3	22.4
CDBP (CC/100gm)	ASTM D5230	92.4	91.5
Sulphur Content (%)	ASTM D 7679	0.97	0.54
Pour density (kg/m ³)	ASTM D 1513	364	358

3.8 Mechanical properties of Various CBs incorporated the natural rubber

The rubber sheets were prepared as per standard ASTM D 3192 composition. ASTM D412 was used to determine the tensile strength and modulus 300 percent of various CBs. PBFS-CB and CTBFS-CB have tensile strengths of 18.4 MPa and 18.0 MPa, respectively (Fig.8). The 300 % modulus of various CBs such as PBFS-CB and CTBFS-CB is 487 MPa and 484 MPa, respectively (Fig.8). Due to the nearly identical BET surface area (Fig.7) and particle size distribution (Fig. 6) in PBFS-CB and CTBFS-CB, the tensile strength and modulus 300 % (Fig.9) are not different. However, minimal difference is observed due to the change in compactness during the preparation process.

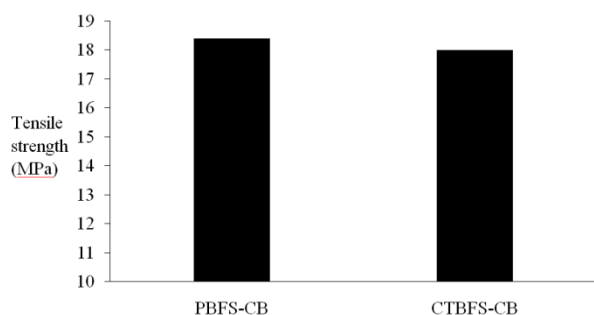


Fig.8 Tensile strength of various carbon black samples mixed in rubber

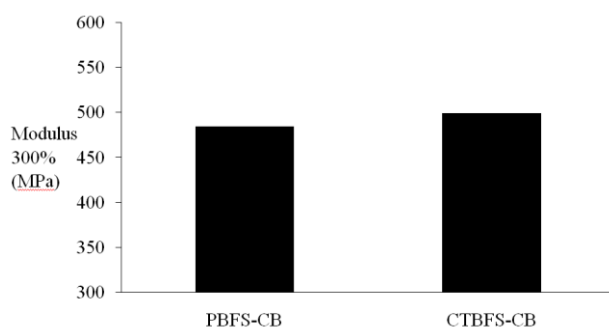


Fig.9 Modulus of various carbon black samples mixed into natural rubber

3.9 Dynamic properties of various CBs incorporated the natural rubber

The dynamic properties of various CBs such as PBFS-CB and CTBFS-CB i.e., abrasion loss and heat build-up (HBU) have been determined in accordance with ASTM D5963 and ASTM D623. PBFS-CB and CTBFS-CB have the abrasion loss of 134 mm³ and 131mm³, respectively (Fig.10). The HBU of various CBs such as PBFS-CB and CTBFS-CB is 24 °C and 26 °C, respectively. The abrasion loss and heat build-up (HBU) are not differed due to the approximately identical tensile strength (Fig.8) and Modulus 300% (Fig. 9) in CB samples.

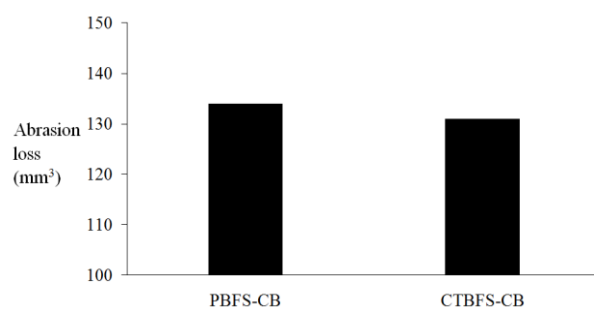


Fig.10 Abrasion loss of various carbon black samples mixed into natural rubber

3.10 Rheological properties of various CBs incorporated the natural rubber

The rheological properties of various CBs, incorporated in natural rubber, such as minimum torque, maximum torque and change in cure rate were examined at 145 °C. The obtained results are illustrated in Table 2. The CTBFS-CB shows slightly fast cure nature than PTBFS-CB due to PBFS has higher percentage of sulphur content and which retards the vulcanization.

4. CONCLUSION

The Physio-chemical Properties of CBs such as PBFS-CB and CTBFS-CB Produced from two different feedstocks, PBFS and CTBFS were successfully examined in this work. Both the CBs chemical and mechanical qualities were tested. The experimental findings demonstrated that good co-relation in aggregate particle size distribution of samples produced with CTBFS and PBFS as feedstock. There are no significant changes observed in surface area of the various CBs. The particle size of different CBs observed 1.30 μm and 1.36 μm. The tensile strength and Modulus 300% are almost same values observed in CBs. The abrasion loss and heat build-up (HBU) are not differed due to the nearly identical tensile strength and Modulus 300% in PBFS-CB and CTBFS-CB.

The eventual AN is relative to surface area of CB. The PBFS-CB and CTBFS-CB have iodine adsorption values of 121.5 mg/g and 120.8 mg/g, respectively whereas the DBP absorption of these CBs is 114.6 and 113.2 cc/100 gm, respectively. The obtained results are comparable for PBFS-CB and CTBFS-CB. The results of the investigation reveal that the influence of different feedstock types can be mitigated technically by enhancing the control of the Carbon black production process. It also proves that technological advancements in the carbon black business may give consistent results regardless of the input material.

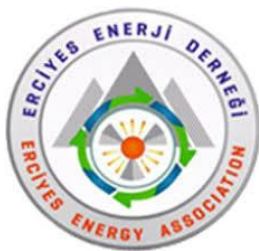
REFERENCES

- [1] Bansal, R. C., Wang, M. J., Donnet, J. B., 1993. Carbon black. Science and Technology, 133.
- [2] Chandrasekaran, V. C., 2010. Rubber as a construction material for corrosion protection: a comprehensive guide for process equipment designers. Publisher: John Wiley & Sons.
- [3] Cheng, W., Liu, Y., Tang, J., Duan, H., Wei, X., Zhang, X., ... & Leng, S., 2020. Carbon content in airway macrophages and genomic instability in Chinese carbon black packers. Archives of Toxicology, 94(3), 761-771.
- [4] Ciobanu, M., Lepadatu, A. M., & Asaftei, S., 2016. Chemical and electrochemical studies of carbon black surface by treatment with ozone and nitrogen oxide. Materials Today: Proceedings, 3, 252-S257.
- [5] Donnet, J., Bansal, R.C., Wang, Meng-Jiao, 2018. Carbon black: Science and technology. Publisher: Taylor Francis. Fourth ed. Academic Press, Waltham.
- [6] Ikram, I., Hashin, A., 2002. Natural rubber biodegradation in soil in relation to the waste disposal of used latex products. In Paper presented at 5th Annual International Conference, 30, 31
- [7] International Carbon Black Association (ICBA), 2016. Carbon black user's guide.
- [8] International Energy Agency (IEA), 2007. Tracking industrial energy efficiency and CO₂ emissions.
- [9] Kaminsky, W., Mennerich, C., Zhang, Z., 2009. Feedstock recycling of synthetic and natural rubber by pyrolysis in a fluidized bed. J. Anal. Appl. Pyrolysis 85(1-2), 334-337.
- [10] Kato, A., Ikeda, Y., Kohjiya, S., 2018. Reinforcement mechanism of carbon black (CB) in

natural rubber vulcanizates: relationship between CB aggregate and network structure and viscoelastic properties. *Polymer-Plastics Technology and Engineering*, 57(14), 1418-1429.

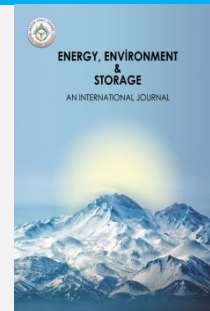
- [11] Lee, S., Kim, K.H. and Lee, Y.S., 2017. Preparation of carbon discs using petroleum-based binder pitch reformed with carbon black. *Carbon letters*, 23, 84-87.
- [12] Lippens, B.C. and De Boer, J.H., 1965. Studies on pore systems in catalysts: V. The t method. *Journal of Catalysis*, 4(3), 319-323.
- [13] Mark, E.J., Erman, B., Eirich, F.R., 2005. *Science and Technology of Rubber*, third ed. Elsevier Academic Press, San Diego; London, 368
- [14] Mark, E.J., Erman, B., Roland, C.M., 2013. *The Science and Technology of Rubber*, fourth edition, publisher : Elsevier ,1-801
- [15] Okoye, C. O., Jones, I., Zhu, M., Zhang, Z., & Zhang, D. (2021). Manufacturing of carbon black from spent tyre pyrolysis oil—A literature review. *Journal of Cleaner Production*, 279, 123336.
- [16] Park, S. J., Kim, J. S., 2000. Role of chemically modified carbon black surfaces in enhancing interfacial adhesion between carbon black and rubber in a composite system. *Journal of colloid and interface science*, 232(2), 311-316.
- [17] Peeten, T.L. (Eds.), *Carbon Black: Production, Properties and Uses*.
- [18] Quan, Y., Liu, Q., Zhang, S., & Zhang, S., 2018. Comparison of the morphology, chemical composition and microstructure of cryptocrystalline graphite and carbon black. *Applied Surface Science*, 445, 335-341.
- [19] Rodgers, B. (Ed.), 2015. *Rubber compounding: chemistry and applications*. CRC press
- [20] .
- [21] Roy, C., Rastegar, A., Kaliaguine, S., Darmstadt, H. and Tochev, V., 1995. Physicochemical properties of carbon blacks from vacuum pyrolysis of used tires. *Plastics, Rubber and Composites Processing and Applications*, 23(1), 21-30.
- [22] Ruble, T. A., 1970. Carbon Black from Petroleum Oil. In: *Advances in Chemistry*. American Chemical Society, Washington DC, 264- 270.
- [23] Shah, A. A., Hasan, F., Shah, Z., Kanwal, N., Zeb, S., 2013. Biodegradation of natural and synthetic rubbers: A review. *International biodeterioration & biodegradation*, 83, 145-157.

- [24] Snowdon, M. R., Mohanty, A. K., & Misra, M., 2014. A study of carbonized lignin as an alternative to carbon black. *ACS Sustainable Chemistry & Engineering*, 2(5), 1257-1263
- [25] Srinivasaraonik, B., Sinha, S. and Singh, L.P., 2021. Synthesis of encapsulation of binary mixture by silica and its performance in pure cementitious system. *Energy Storage*, 3(3), 229.
- [26] Srivastava, M., Singh, I.D., Singh, H., 1999. Structural characterization of petroleum-based feedstocks for carbon black production. *Petrol. Sci. Technol.* 17(1-2),67-80.
- [27] Standard Test Method for Carbon Black—Iodine Adsorption Number, 2021. American Society for Testing and Materials (ASTM), ASTM D1510
- [28] Standard Test Method for Carbon Black—Oil Absorption Number (OAN), 2021. American Society for Testing and Materials (ASTM), ASTM D2414
- [29] Standard Test Method for Carbon Black—Oil Absorption Number of Compressed Sample (COAN), 2019. American Society for Testing and Materials (ASTM), ASTM D3493
- [30] Standard Test Method for Rubber Property—Abrasion Resistance (Rotary Drum Abrader), 2019. American Society for Testing and Materials (ASTM), ASTM D5963.
- [31] Standard Test Methods for Vulcanized Rubber and Thermoplastic Elastomers—Tension, 2021. American Society for Testing and Materials (ASTM), ASTM D412.
- [32] Wang, G., Yan, K., 2011. Carbon black for energy storage and conversion, in: Sanders, I.J.,
- [33] Wang, M., Gray, C., Reznik, S., 2003. *Carbon black*. John Wiley & Sons, 761–803.
- [34] Wibawa, P.J., Nur, M., Asy'ari, M. and Nur, H., 2020. SEM, XRD and FTIR analyses of both ultrasonic and heat generated activated carbon black microstructures. *Heliyon*, 6(3), 03546.
- [35] Zhou, J., Luo, A. and Zhao, Y., 2018. Preparation and characterisation of activated carbon from waste tea by physical activation using steam. *Journal of the Air & Waste Management Association*, 68(12), 1269-1277.
- [36] Farida, E., Bukit, N., Ginting, E.M. and Bukit, B.F., 2019. The effect of carbon black composition in natural rubber compound. *Case Studies in Thermal Engineering*, 16, 100566.



Energy, Environment and Storage

JournalHomepage: www.enenstrg.com



Testing of Ethylene Glycol Ketal, Dioxane and Cyclopentanone as Components of B10, B20 Fuel Blends

Ibrahim Mamedov^a, Gular Mamedova^a, Nargiz Azimova^a

^aBaku State University, Faculty of chemistry, Z. Khalilov 23, Baku, Azerbaijan

ABSTRACT. The aim of the present work was to the preparation of biodiesel from sunflower oil and methanol by the transesterification reaction in the presence of the KOH. The conversion was 95% using a 1:3 molar ratio of oil to alcohol at 65°C. Important fuel physical properties of B10 and B20 fuel blends with (or without) oxygenated additives by the ASTM standards had been investigated. Based on the obtained results is noted that the fuel blend B10 and B20 with oxygenated additives has greater potential for diesel engines than, B100 and fossil diesel. The best result was demonstrated B10+1.4-dioxane fuel blend among the studied fuels.

Keywords: transesterification, biofuel, biodiesel, ketal, oxygenated additives

Doi: <https://doi.org/10.52924/RBCY7188>

1. INTRODUCTION

Today one of the most important key factors to affect the world economy and politics is the petroleum and gas resources which are the main sources of world energy supply. In the modern world to meet the needs of energy different resources have been developed. But our planet has a lot of environmental problems with the exhaust toxic emission from the usage of fossil fuels. Another problem is the exhaustion of petroleum, natural gas, etc. resources. Therefore, alternative energy sources mostly biofuels are receiving more attention [1-4].

From the alternative type of fuels, biodiesel is a renewable resource consisting of fatty acid alkyl monoesters derived from vegetable oil, waste animal fats, or waste cooking oil. Important is need to note, at the combustion of biodiesel does not emit toxic substances that cause environmental problems due to the absence of aromatic, nitrogen and sulfur compounds [5-8].

In comparison with conventional diesel fuels, the oxygen in biodiesel may promote more complete combustion and thus reduce particulate matter, carbon monoxide and total hydrocarbons in ignition engines. According to a review of emission data for heavy-duty engines published by EPA (Environmental Protection Agency of USA 2002), from diesel to B20, carbon monoxide, toxic hydrocarbons and particle matters decreased by 13, 20 and 20 % respectively [9-11].

Considering the above, in the presented work, the transesterification reaction of sunflower oil with methanol in the presence of KOH was carried out. The important operational properties of B10 and B20 fuel blends on the

basis of FAME were tested in the presence (or absence) of ethylene glycol ketal (EGK), 1,4-dioxane (DO) and cyclopentanone (CP). The oxidation properties of B10 and B20 fuel blends were estimated by using NMR data.

2. EXPERIMENTAL MATERIALS AND INSTRUMENTATION

All the chemicals for the synthesis of ethylene glycol ketal and dioxane were obtained from commercial sources (Aldrich) and used as received (Figure 1, 2). Samples of diesel fuel, sunflower oil were purchased at a fuel station and markets in Baku, Azerbaijan. The B10 and B20 fuel blends with (or without) oxygenated additives were prepared by mixing diesel and biodiesel.

NMR experiments have been performed on a BRUKER FT NMR spectrometer (UltraShield™ Magnet) AVANCE 300 (300.130 MHz for 1H and 75.468 MHz for 13C) with a BVT 3200 variable temperature unit in 5 mm sample tubes using Bruker Standard software (TopSpin 3.1). The 1H and 13C chemical shifts were referenced to internal tetramethylsilane (TMS); the experimental parameters for 1H: digital resolution = 0.23 Hz, SWH = 7530 Hz, TD = 32 K, SI = 16 K, 900 pulse-length = 10 μs, PL1 = 3 dB, ns= 1, ds= 0, d1 =1 s; for 13C: digital resolution = 0.27 Hz, SWH = 17985 Hz, TD = 64 K, SI = 32 K, 900 pulse-length = 9 μs, PL1 = 1.5 dB, ns= 100, ds= 2, d1= 3 s. NMR-grade CDCl₃ was used for the analysis of ethylene glycol ketal and fuel blends.

The purity of the synthesized ethylene glycol ketal confirmed by thin-layer chromatography (TLC) on commercial aluminum-backed plates of silica gel (60 F254), iodine vapor was used as a visualizing agent, eluent- 5:2 hexane/ethyl acetate.



Figure 1. Dioxane and ethylene glycol ketal



Figure 2. The preparation of the ethylene glycol ketal

The procedure for preparation of biodiesel

Sunflower biodiesel (B100) was obtained by dissolving 0.69 g KOH in 37.5 ml of methanol (CH₃OH) without heating (at room temperature). After complete dissolution, 50 g of oil was added to this mixture. The reaction was carried out in a conical flask equipped with a reverse refrigerator and magnetic stirrer for 6 hours at 65 °C (rotation speed was maintained at 1000 rpm). After stirring, the reaction mass was aged for at least 12 hours in a dividing funnel. The reaction mass was divided into 2 layers using a dividing funnel: the upper layer contained biodiesel, the lower layer-glycerine. Untreated biodiesel was repeatedly washed with water in order to remove catalysts. The conversion rate was 95% when using the molar ratio of oil to methanol 1:3 (Figure 3).



Figure 3. The preparation of the biodiesel



Figure 4. Biodiesel synthesized from sunflower oil and its blends were characterized in accordance with the American Standard of Testing and Materials (ASTM) methods.

The procedure for preparation of ethylene glycol ketal

A mixture of 30 g of pure ethylene glycol, 100 ml of cyclopentanone (in Figure 5), 0.75 g of p-toluene sulfonic acid (PTSA) was placed in a 500 ml conic flask fitted a reflux condenser and magnetic stirrer. The reaction mixture was stirred under 100°C for 5 working days. After the completion of the reaction mixture was neutralized with 0.5 g sodium acetate. In the next stage filtration and evaporation of the cyclopentanone had been carried out. The ketal was obtained by vacuum distillation, yield 65% (Figure 2).

Figure 5. Mixture of hydroxyl and cyclopentanone

3. RESULTS AND DISCUSSION

In our previous works [12-14], the preparation of methanol, ethanol biodiesels catalyzed by a new ionic liquid system (or KOH) and testing of their operational properties had been informed. This work is devoted to the preparation of methanol biodiesel from the sunflower oil, testing their different exploitation properties with (or without) the ETG, DO and CP additives.

As known from the literature oxygenated compounds, such as glycerol ketals, pine oil (PO), essential oils, etc. can be used as a fuel additive to reduce particulate emission and to improve the cold flow properties of liquid transportation fuels. It helps to reduce gum formation, improves oxidation stability, etc. [15, 16].

The used feedstock sunflower physicochemical properties are shown in Table 1.

Table 1. Major fatty acids and physical properties of the refined sunflower oil

Fatty acid composition (wt.%)	16:0	18:0	18:1	18:2
		3.5–7.6	1.3–6.5	14–43
Acid value (mg of KOH/g)	0.28±0.5			
Saponification value (mg KOH/g)	193.3±0.5			
Iodine value (g I ₂ per 100 g)	121.4±0.5			
Viscosity (cP)	34.1±0.5			
Flash point (°C)	265			
Pour point (°C)	+12			
Density (g/cm ³)	0.9186			

Considering the above indicated, the properties B10 and B20 blends in presence of EGK, DO and CP was studied. The physical properties of the diesel, sunflower biodiesel (B100), B10 and B20 blends with (or without) oxygenated additives were investigated and the results are shown in Tables 2, 3.

Table 2. The physical properties of B10, B20, B100 and diesel fuels

Properties	ASTM Methods	ASTM		diesel	B10	B20	B100
		diesel	biodiesel				
Relative density at 20°C, g/cm ³	D1298	0.8-0.84	0.86-0.9	0.837	0.848	0.855	0.88
Viscosity at 40°C, mm ² /s, min-max.	D445	2-5	3.5-5.0	3.44	3.54	3.60	4.1
Flash point, °C, min.	D93	65	>120	70	114	105	174
Cloud point (°C)	D2500	-12	<20	7	3	5	+12
Pour point (°C)	D2500	-15	<15	0	-7	-5	+6
Iodine value g (I ₂)/100 g	-	60-135	<120	1.58	44.5	45.7	110.5
Sulfur, ppm, max.	D 975-14	15	15	50	35	33	0
Water and sediment, vol%, max.	D 975-14	0.05	0.05	0	0	0	0
Copper corrosion, 3 hr at 50°C, max.	D 975-14	№3	№3	№2	№1	№1	№1
Cetane number, min.	D 975-14	40	47	43	43.7	44.1	48.5

As seen in Tables 2 and 3 density decreased for all B10 and B20 fuel blends. The density is a factor governing the quality of crude petroleum, it is an uncertain indication of petroleum product quality unless correlated with other properties. But, kinematic viscosity significantly decreases for all fuel blends in the presence of 5% oxygenated compounds in the blends. Minimal kinematic viscosity has the B10+DO fuel blend (3.13 mm²/s). The significantly decreasing viscosity positively influences the flow and sprays characteristics in the engine [2, 4].

The flashpoints are decreased for the biodiesel blends than for pure biodiesel (B100). The best flashpoint was demonstrated B10+DO fuel blend with the 78°C. The cloud and pour points for fuel blends at the presence of

oxygenated additives were decreased. The best cloud and pour points were typical for the B10+DO blend.

The amount of sulfur significantly decreased as the percentage of biodiesel and oxygenated compounds in blends from 50 up to 33 ppm, which is very important for the environment and human health. As shown in our experimental results, water, sediment, also copper corrosion parameters are excellent [8].

The oxidation stability of diesel and B10 and B20 blends before and after oxidation was estimated by the ratio of NMR integral intensity of the naphthenic-paraffinic region at 0.5-4.5 ppm. to the olefinic-aromatic region at 4.5-6.0 ppm. and 6.6-9.0 ppm. accordingly (Table 4).

Table 4. The oxidation stability of diesel and B10 and B20 blends

	diesel	B10	B10	B20	B10	B20	B10	B20
		FAME	FAME+EGK (5%)	FAME+EGK (5%)	FAME+DO (5%)	FAME+DO (5%)	FAME+CP (5%)	FAME+CP (5%)
Before (OS _{NMR})	9.89	11.28	8.95	8.21	15.71	13.32	11.6	10.31
After (OS _{NMR})	5.88	5.31	6.59	5.41	8.39	7.59	6.15	5.78

As seen in Table 4, high oxidation stability has the B10+DO fuel blend. The oxidation stability of other oxygenated fuel blends also is more than that of diesel and B100 fuel blends during the oxidations at 16 hours, at 95°C. This is due to the fact that oxygenated additives protect the fuel from oxidation.

Considering the above indicated, we note that the B10+DO fuel blend has low kinematic viscosity (3.13 mm²/s), flashpoints temperature (78°C), high oxidation stability and best exploitation properties demonstrated.

4. CONCLUSIONS

The properties of diesel, B10, B20, B100 fuel blends with (or without) oxygenated additives were investigated on the ASTM (Figure 4) standards.

Obtained results have demonstrated improvements of the important physical properties- such as density, viscosity, amount of sulfur, copper corrosion, flash-, pour- and cloud points for B10, B20 fuel with oxygenated compounds.

Summarizing the obtained data, we can note that the fuel blends B10, B20 with oxygenated compounds have greater potential for diesel engines than pure biodiesel (B100) and commercial diesel fuel. The best result was demonstrated B10+DO fuel blend among the studied fuels.

REFERENCES

- [1] Oner, C., Altun, S. Biodiesel production from inedible animal tallow and an experimental investigation of its use as alternative fuel in a direct injection diesel engine, *J Appl Phys.*, 86(10), 2114–2120, 2009.
- [2] Aksoy, F. The effect of opium poppy oil diesel fuel mixture on engine performance and emissions, *Int J. Environ. Sci. Tech.*, 8(1), 57–62, 2011.
- [3] Meher, L.C., Vidya, D.S., Naik, S.N. Technical aspects of biodiesel production by transesterification-a review, *Renew. Sust. Energy Rev.*, 10, 248-268, 2006.
- [4] Miriam, D.T, Gonzalo, J., Jose, A.M., Elisabet, P., Mario, S. Glycerol ketals: Synthesis and profits in biodiesel blends, *Fuel*, 94, 614-6162, 2012.
- [5] Ma, F., Hanna, M.F. Biodiesel production: a review, *Bioresour. Technol.*, 70, 1–15, 1999.
- [6] Zheng, M, Mulenga, M.C., Reader, G.T., Tan, Y., Wang, M., Tjong, J. Neat biodiesel fuel engine tests and preliminary modeling, *SAE Technical Paper Series*, 01, 1-16, 2007.

[7] Nwafor, O.M.I. Emission characteristics of diesel engine operating on rapeseed methyl ester, *Renew. Energy*, 29, 119-129, 2004.

[8] Prasad, T.H., Reddy, K.H.C., Rao, M.M. Performance and exhaust emissions analysis of a diesel engine using methyl ester of oil with artificial neural network aid, *Inter. J. Engineer. Tech.*, 2, 23-27, 2010.

[9] Environmental Protection Agency of USA (2002) A comprehensive analysis of biodiesel impacts on exhaust emissions. Draft technical report (EPA420-P-02-001) web. <https://19january2017snapshot.epa.gov/www3/otaq/model/s/analysis/biodsl/p02001.pdf>.

[10] Shahmirzae, H.J., Fallahipahan, M., Hashemi M. G., Chen, L. Performance analysis of Diesel engines fueled by biodiesel blends via thermodynamic simulation of an air-standard diesel cycle, *Int. J. Environ. Sci. Technol.*, 11, 139-148, 2014.

[11] Lee, H.V., Juan, J.C., Taufiq-Yap, Y.H., Kong, P.C., Rahman, N.A. Advancement in heterogeneous base catalyzed technology: An efficient production of biodiesel fuels, *J. Renew. Sust. Energy*, 7, 1-47, 2015.

[12] Mamedov, I., Huseynova, S., Javadova, O., Azimova, N. Pine oil and glycerol ketal as components of B10 fuel blends, *Indian Journal of Chemical Technology*, 29, 442-447, 2022.

[13] Mamedov, I.G., Javadova, O.N., Azimova, N.V. Preparation of diesel fuel blends and study of their physical properties, *Proc. Univer. Appl. Chem. Biotech.*, 2, 332-338, 2020.

[14] Mamedov, I., Huseynova, S., Javadova, O., Azimova, N., Huseynova, R., Gasimova, Sh, Testing of pine oil and glycerol ketal as components of B10 fuel blend, *Energy, Environment and Storage*, 2(1), 11-14, 2022.

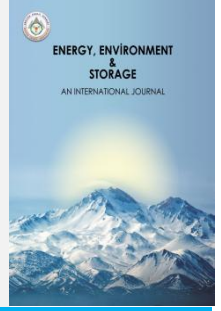
[15] Nanda, M.R., Zhang, Y., Yuan, Z., Qin, W., Ghaziaskar, H.S., Xu, C.C. Catalytic conversion of glycerol for sustainable production of solketal as a fuel additive: A review, *Renew.Sust. Energy Rev.*, 56, 1022-1031, 2016.

[16] Prakash, T., Geo, V.E., Martin, L.J., Nagalingam, B. Evaluation of pine oil blending to improve the combustion of high viscous (castor oil) biofuel compared to castor oil biodiesel in a CI engine, *Heat Mass Trans.*, 55, 1491-1501, 2019.



Energy, Environment and Storage

JournalHomepage: www.enenstrg.com



Investigation of the Performance Changes of the Savonius Wind Turbine Rotors with the Same Front View Area of Look by Change of the Aspect Ratio

Mahmut Burak Akkus¹, Zeki Haksever² and Süleyman Osmanlı³

¹Erciyes University, Faculty of Engineering, Department of Mechanical Engineering, Kayseri, Türkiye

¹mbakkus54@gmail.com, ORCID:0000-0002-4561-7093,

²Erciyes University, Faculty of Engineering, Department of Mechanical Engineering, Kayseri, Türkiye

²zhaksever@gmail.com, ORCID: 0000-0001-7037-4540

³Van Yuzuncuyil University, Faculty of Engineering, Department of Mechanical Engineering, Van, Türkiye

³steksin@yyu.edu.tr, ORCID: 0000-0001-8854-0332

ABSTRACT. In this study, Savonius type wind turbine rotors with the same front view area were produced with 3D printers by changing their aspect ratios, and then both experimental and numerical analyzes were carried out according to them attaching end plate and without end plate situations. The wind tunnel in the university was used in the experimental analysis. For numerical analysis, rotors and wind tunnels modeled in SolidWorks CAD program were analyzed in Ansys Fluent program. The analyzes made are for imaging purposes only, and the results in the experimental analyzes are accepted as correct. The reduction of aspect ratios in the uncapped analyzes decreased the overall efficiency, but the opposite effect was observed when the analyzes were repeated with the end plate. In addition, while negative pressure was observed in the rotors made without end plate (bare case) in the digital images, this situation was not seen in the analyzes made with the end plate.

Keywords: Wind Turbines, Savonius, Tip Speed Ratio, Power Factor, Pressure

Doi: <https://doi.org/10.52924/WFVI2347>

1. INTRODUCTION

Humanity has needed energy to live for generations. Some attempts have been made to do this, both from the nutrients they get for survival and to make their daily life comfortable. Especially after the industrial revolution, to meet the rapidly increasing energy need, this need has been tried to be met by first using water vapor and then fossil fuels. However, as a result of this, the rapid deterioration of the world ecosystem has made it possible to switch to alternative energy production methods. The reason for this is the emergence of gases that disrupt the ecosystem and pollute the atmosphere while obtaining energy from fossil fuels. The electrical energy that we use frequently today can be obtained through various transformations, even if it is not found directly in nature. In electricity generation, natural resources are always produced by using a turbine or turbine group with subsequent generators [1-2].

Due to the increasing energy demand and climate change based energy crises recently, electricity generation from other natural sources has become increasingly common. But still, fossil fuels are widely used due to the need of improvement of renewable energy implication [3].

Although each of the researched subjects in this study are included in the literature studies separately. Akkuş et al. [4] experimentally and numerically examined the performance that can occur by adding caps of different diameters to Savonius rotors with different blade structures with approximately the same area and observed that caps with a larger rotor diameter increase the performance significantly. Ali [5] conducted a study experimentally comparing Savonius rotors at low speeds according to the number of blades. In the experimental study, 2- and 3-bladed rotors were produced with certain calculations, their performances were compared under the same test conditions, and it was decided that 2-bladed rotors were more efficient. Altan et al. [6] produced the Savonius wind turbine rotors using 3D printers and then investigated the effect of the change on the performance of the change, which is caused by adding plates of specified dimensions to their blades, both experimentally and numerically. According to the results obtained from the experiments, it was concluded that the compression of the flow in the blades decreased, and the performance of the rotor increased. It was observed that the power coefficient in the rotor increased by 20 percent when the (1/r) ratio was adjusted to 0.3, the (s/r) ratio to 1, and the added plate angle as 135 degrees. Zhao et al. [7] aimed to increase the

*Corresponding author: youremail@mail.com

power coefficient with the helical Savonius rotors they designed, although the power coefficient of the classical Savonius rotor is about 0.15. In this development, aspect ratio (H/D_{Rotor}), overlap ratio, and helix angle were used as variables. As a result of the study, while the aspect ratio was 6, the overlap ratio was 0.3 and the helix angle was 180 degrees, the optimum power coefficient increased to 0.2 (the tip speed ratio was 0.75 at this time). In addition, the starting torque value was better than the conventional rotor. Kharade et al. [8] tried to explain experimentally and theoretically the methods of increasing the overall efficiency of the rotors of vertical axis wind turbines by optimizing them. For Savonius turbines, although not much different from the above-mentioned efficiency-increasing methods, the performance of Savonius rotors with helical blade structures formed by the change of twist angles, according to the number of blades, was examined. As a result of this study, the power coefficient of 2-bladed rotors ($C_p = 0.53$) was found to be greater than that of 3-bladed rotors ($C_p = 0.36$). Zemamou et al. [9] carried out studies to increase the power coefficient of the classical savonius rotor (classic savonius C_p range varies between 0.1 and 0.25) and because of the geometric improvements they made, they increased the power coefficient to 0.273. Gül and Kolip [10] achieved better results with the split blade designs of the Savonius rotor that they designed, which open and close according to the wind direction, compared to the power coefficient of the classical Savonius rotor ($C_p = 0.38$) and an improvement of 40 percent was observed compared to the other designed models. Jeon et al. [11] investigated the performance change in the wind tunnel by adding caps in different shapes (4 types) to savonius rotors with helical blade structure and changing the diameters of these end plates. In addition, they examined the rotor performance in the without end plate state. According to the results obtained, while the power coefficient values of all of them up to 0.2 are close to each other, after 0.2 it is concluded that the rotor with the end plate is higher in terms of power coefficients than the case without the end plate. In this result, it can easily be seen that it is more than double if the rotor, which is in the full-circle capped state, is compared according to the highest values of the power coefficients compared to its without end plate state.

Although the subjects investigated in this study are separately included in the literature studies, for example, Zhao et. get. [7], the performance changes of the rotors formed by the change of the H/D_{Rotor} ratios have been examined, and the examination of the produced rotors without end plate condition according to their with end plate condition is given in Akkuş [4] and Jeon [11]. No study was found in which the investigated parameters were compared together. Accordingly, they evaluated the results by comparing their studies according to the data they obtained.

2. MATERIALS AND METHODS

2.1 Method

All of the produced savonius rotors were created by 3D printers. 3D printers have become frequently used in daily life due to their outstanding performance in various

industries [12]. The produced rotors were investigated experimentally and numerically. Experimentally, it was carried out in the wind tunnel in the Aerodynamics Laboratory of the Faculty of Aeronautics and Astronautics of Erciyes University. As a result of numerical analysis, the experimental setup designed in the cad program was created in the Fluent program. The numerical analysis part was carried out with the data taken from the experimental analysis. More detailed information is given in the numerical analysis section below.

2.2 Material

The infill ratio is low so that the rotors are not heavy in terms of aerodynamics. Production was carried out by adhering to the production tolerances of the rotor, depending on the calibration of the printer used. In addition, the end plates are made of medium-density fiberboard material with laser cutting.

Table 1. Printing Parameters of 3D Printed Rotors.

Aspect ratio [H/D_{rotor}]	Filament used	Nozzle Temperature [°C]	Table Temperature [°C]	Print Speed [mm/s]	Weights [gr]	Solidity ratio [Infill]	Layer Thickness [mm]	Print Time [Hour]
0.75	esun pla+ [White]	210	20	30	193	10%	0.2	27.35
1	esun pla+ [White]	210	20	30	188	10%	0.2	26.20
1.25	K Camel pla [Black]	210	20	30	198	10%	0.2	25.30
1.5	esun pla+ [White]	210	20	30	189	10%	0.2	25

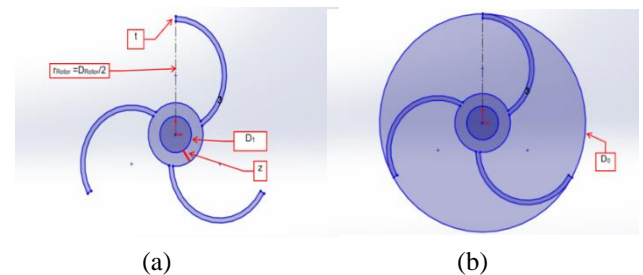


Figure 1. (a) Without endplate and (b) With endplate of the designed rotors (Schematic representation)



Figure 2. Height of designed rotors (Schematic representation)

Table 2. Geometric parameters of 3D printed rotors.

Aspect ratio [H/D Rotor]	Rotor Diameter [D Rotor -mm]	Rotor Cover Diameter [D 0 -mm]	Rotor/Shaft Bore diameter [D 1 -mm]	Rotor Height [H-mm]
0.75	209,761	209,761	10	157,321
1	181,659	181,659	10	181,659
1.25	162,480	162,480	10	203,101
1.5	148,323	148,323	10	222,486

Table 3. Geometric parameters of 3D printed rotors (Continued)

Aspect ratio [H/D Rotor]	Rotor Covers Wall Thickness [mm]	Wing Wall Thickness [t-mm]	Rotor Hole Thickness [z-mm]	Number of Wings
0.75	2.9	5	5	3
1	2.9	5	5	3
1.25	2.9	5	5	3
1.5	2.9	5	5	3

Front view area,

$$A_{front\ view} = H * d_{rotor} \quad (1)$$

where H is the turbine height.

Mechanical power,

$$P_{turbine} = (T * \omega_{turbine}) \quad (2)$$

where T is the torque and ω is the Turbine angular velocity.

Wind power,

$$P_{wind} = (\rho A_{front\ view} V_{wind}^3) / 2 \quad (3)$$

where ρ is the density and V_{wind} is wind speed.

Tip speed ratio,

$$TSR = (\omega_{turbine} * (d_{rotor}/2) / V_{wind}) \quad (4)$$

Power coefficient,

$$Cp = (P_{turbine}/P_{wind}) \quad (5)$$

The values obtained by analyzing the produced rotors in the experimental environment will be displayed in the graph called TSR/Cp. Above are the theoretical equations related to this subject. The TSR is also known as the tip speed ratio and is the ratio of the linear speed of the turbine to the speed of the wind. Cp is known as the performance or power coefficient and is the ratio of the mechanical power produced by the turbine to the flow power in the wind. The optimum design point is equivalent to the maximum value of the coefficient of performance. produced above the front view area of all the rotors was determined as 330 cm² (0.033 m²). The main purpose of this study is to examine the performance

changes in the rotors produced by changing the aspect ratios, both with their end plates (the ratio of the end plates of all rotors is determined as $D_{Rotor} / D_0 = 1$) and without the end plate. The fact that all the blades in the produced rotors are straight blades is due to the poor calibration of the 3D printer. Therefore, the resulting Cp values may be lower than those in the literature. In the same way, since the problem of the 3D printer not pulling the filament on time, there were problems in the integrity of the structure, but in general, the structures are suitable for aerodynamic analysis.

3. RESULTS

3.1 Experimental Analysis

As mentioned before, the experimental analysis part was carried out in the wind tunnel at the Laboratory of Erciyes University. The dimensions of the tunnel are in meters known as 2.3 m x 1.71 m x 10.6 m, respectively. In addition, the inlet and outlet cross-sections of test section in meters are given as 0.57 m x 0.57 m and 0.59 m x 0.59 m, respectively. This wind tunnel can operate in the range of 3-33 m/s. There is a 15-kW fan in the tunnel. The general view and cad view are given below.



Figure 3. Wind tunnel main view (Erciyes University Faculty of Aeronautics and Astronautics Aerodynamics Laboratory)

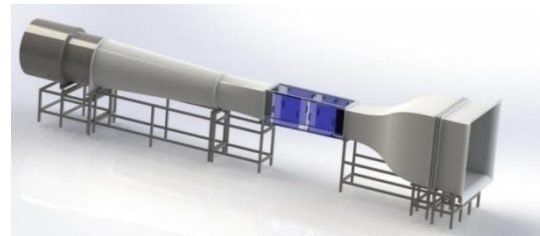


Figure 4. Wind tunnel street view [13]

The laboratory temperature was 15 °C, the density of the air was 1.089 kg/m³, and the kinematic viscosity value was 1.78×10^{-5} kg/m·s. The wind speed for the experiments conducted at a constant 10 m/s.

The experimental procedure can be listed as given the rotors were first attached to a carbon-made rod without end plates, and then one end was mounted in the torque meter slot below and the other end was mounted on the

top cover of the tunnel. Then the tunnel was started and waited until the fan reached 10 m/s wind speed. When it reached sufficient speed, the rotors were first intervened manually and then rotated by the wind. Then, the free load of each of them was calculated and the torque (in Nm unit) and angular velocity (in rpm unit) provided by the rotor was read from the torque meter by descending from that load at certain intervals. The rotors that were tested without the end plate were then re-tuned with the end plates attached (the diameter of the caps is equal to the diameter of the rotor). TSR/C_p graphics were obtained when the values obtained in the table prepared on the computer were entered. The test results for the rotors in the wind tunnel, both with and without the end plate, are shown below.

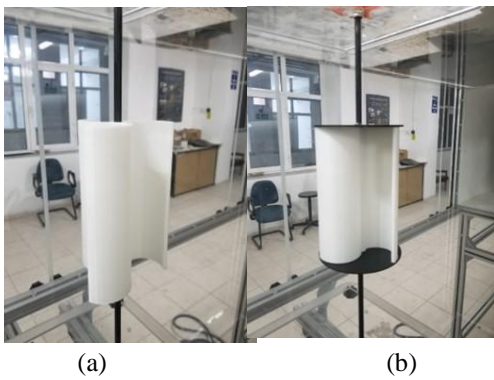


Figure 5. Rotor with 1.5 aspect ratio (a- Without end plate, b- With end plate)

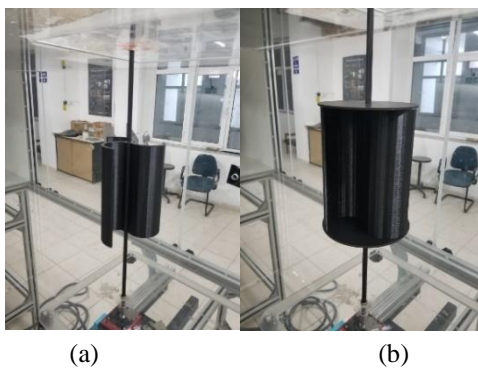


Figure 6. Rotor with 1.25 aspect ratio (a- Without end plate, b- With end plate)

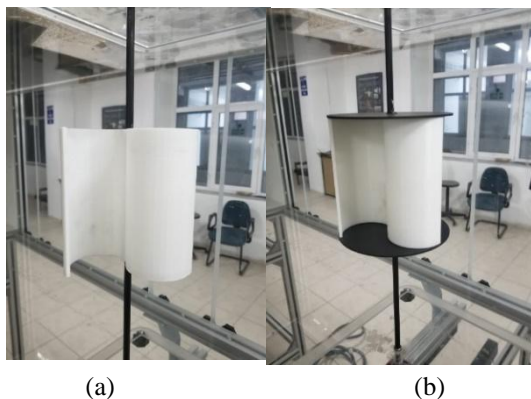


Figure 7. Rotor with 1 aspect ratio (a- Without end plate, b- With end plate)

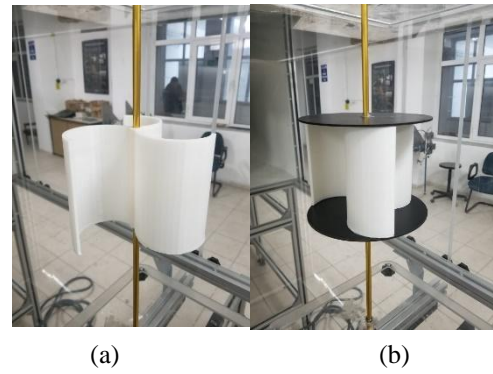


Figure 8. Rotor with 0.25 aspect ratio (a- without end plate, b- With end plate)

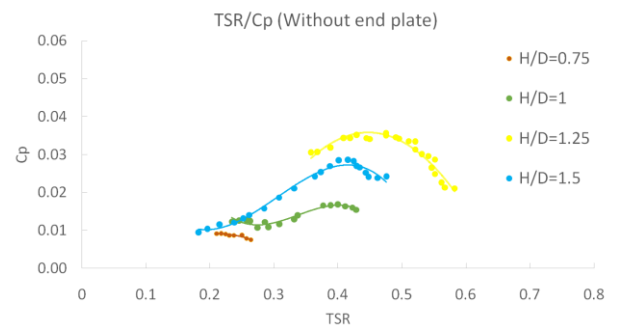


Figure 9. TSR/C_p graph of rotors (Without end plate)

As can be seen from here, the power coefficients increase significantly as the aspect ratio (H/D) of the rotors increases. In particular, rotors with ratios of 1.25 and 1.5 showed outstanding performance compared to rotors with ratios of 0.75 and 1. Their production challenges and the ensuing weight disparities in performance may also have an impact on how well they perform due to the inferior quality of the filament used to manufacture that rotor compared to the others. In addition, the rotor with a ratio of 1.25 in terms of print quality is better than the others. However, since its compatibility with the 3D printer being printed is better than the others, it is possible to print more smoothly and have better power coefficients accordingly. Another factor affecting their overall performance is that rotors with a ratio of 1.5 and 1.25 have more torque than rotors with a ratio of 0.75 and 1. at the same speed. For example, if the rotors with 1.25, 1.5, and 1 ratio according to their performance are compared for approximately 420 rpm, the rotor with the lowest ratio of 1 followed by 1.5 and the rotor with the highest torque value was 1.25. In addition, the high torque also affected the pressure values that the rotors met due to air at the same rate. This can be given to the relationship between the magnitude of the thrust in the torque equation and the radius of the rotors. In addition, the increase in this pressure caused an increase in the power coefficient. This can be seen in the pressure graphs in the numerical analysis below.

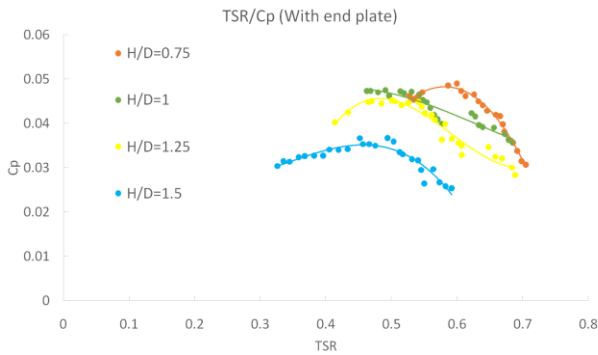


Figure 10. Variation of TSR/C_p (With end plate)

At this time, as the aspect ratio of the rotors becomes smaller, the difference between the power coefficients was small compared to bare case, but it still increased the power coefficients. Here, rotors with a ratio of 0.75 to 1 performed exceptionally well compared to rotors with a ratio of 1.25 to 1.5. Although all rotors have increased their performance compared to their uncapped condition, especially the rotors with the ratios of 1.5 and 1.25 could not increase as much as the rotors with the ratios of 0.75 and 1. The feature that increases the torque in their general performance is the increase in torque and the increase in pressure due to the addition of the effect of the cap on the rotors to the relationship between the thrust force and the radius. A point that should be noted here is that when their performance is compared to their uncapped situation, a torque increase of almost 3 times has been observed for their graphics, especially in the rotors with the ratios of 1 and 0.75, both in the without end plate and with end plate conditions at similar revolutions.

3.2 Numerical Analysis

Numerical analysis was carried out in the ANSYS FLUENT program, as mentioned before. The relevant models were modeled in an external CAD program and transferred to the Ansys program and then to the Fluent part. Since the deviation in the dimensions of the wind tunnel will disrupt the mesh layout, the average of both the entrance and the exit of the tunnel is modeled as 0.58 m x 0.58 m in meters. The total length of the tunnel is 2.7 meters, and the modeled area (rod) is positioned at a distance of 0.9 meters from the entrance part so that the rotors can rotate. In addition, the dimensions of the part called the rod are a cylinder with a radius of 0.15 meters and a height of 0.3 meters, and it is modeled in such a way that it can be placed easily in all rods. The initial layout of the rotor blades is shown below, with the rotor with an aspect ratio of 1.5 as an example model, without end plate. In addition, the hole part, which is suitable for connecting the rotors with a rod as in the experimental analysis, was filled with the extrusion command while creating the cad model of the rotors. Otherwise, it affects the analysis result, and it is modeled in this way since it is seen as if the fluid is passing through the hole in the display of the flow profiles.

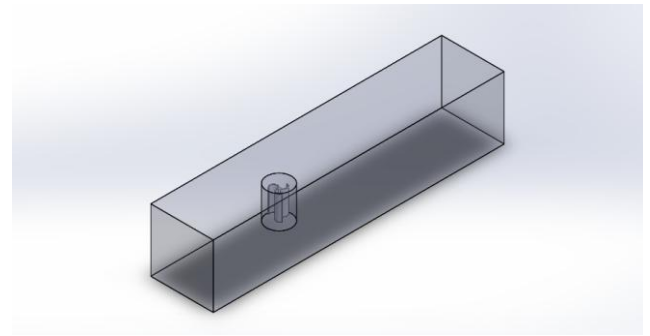


Figure 11. Representation of the model to be used in the analysis (Rotor with 1.5 aspect ratio)

If the analysis will be made here and which parameters will be taken as a basis in such analyzes, the first two rotors with the best TSR/C_p points -the aspect ratios of 1.5 and 1.25 for the ones without end plate, the rotors with the aspect ratio of 0.75 and 1 for the end plates- steady were analyzed. In addition, additional steady analyzes were created for flow monitoring purposes to examine the performance of the rotors at the same angular velocities in terms of comparing each other (with and without end plate in their groups) according to the differences in the experimental results. It is determined that these rotors are 588 rpm in their capped condition and 420 rpm in their uncapped condition. However, the point to be noted here is that the rotor, which has a 0.75 ratio in uncapped situations, performs worse than the others, so it will not be displayed in a capless state. The velocity and pressure contour images taken in each of these analyzes are given below. It is not possible to carry out the analysis within the scope of the assignment, as the validation processes will be quite long. In addition, this method was used because the validations should have reached the appropriate mesh structure and mesh independence, and the results should be as close to the data obtained from the experiments as possible.

Required meshstructures, name definitions, and required values are shown in the meshtable below. Since the reduction of meshes increases both the time and the overall number in the analysis, the smallest possible meshes were discarded and corrected in the polyhedral mesh part in a fluent environment. Also meshes Ansys fluent It was made following the quality values found in the [14] guideline, and the quality values were created close to the limits in this guide.

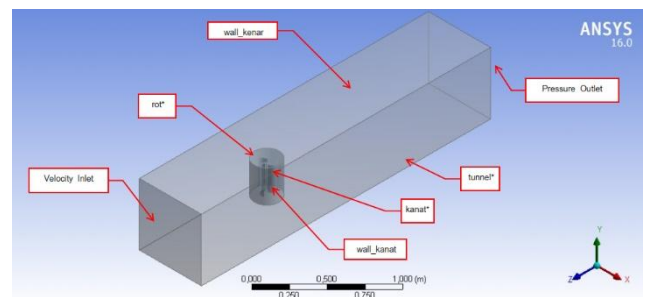


Figure 12. Naming the model to be used in the analysis (Rotor with 1.5 aspect ratio)

The nomenclature with an asterisk on them represents the geometric names, and the rest represent the nomenclature to be used in the analysis. Interface definitions are named between the rod and tunnel surfaces. It has been said before that after the required mesh quality values are provided, pressure-based steady analyzes are made in the Ansys /Fluent program. Since there will be airflow inside the modeled tunnel, the gravitational acceleration is not that effective. Therefore, the gravitational acceleration part remained closed. The input values of the analyzes to be performed at a steady state were taken from the experimental data.

SST k- ω model, which can solve aerodynamic analyzes better than other models based on recent academic studies [15]. When the necessary data were entered on the rod (available in the mesh table), the element that will rotate as intended, the entrance and sections of the tunnel, the analyzes were started and according to the result, both the velocity and pressure contours of the analyzes were taken and transferred here.

Table 4. Mesh parameters of rotors prepared for numerical analysis (All mesh commands not mentioned here are left in standard settings in the program).

Mesh Table			
Aspect ratio (H/ D _{rotor})	General Mesh Method	Local Mesh Method	Inflation (Boundary Layer) Method
0.75 - Without End Plane	Relevance-100/ Relevance Center-Fine / Smoothing -High	Sizing (rot - all body) - 5mm	smooth Transition - 20 Layers
0.75 - With End Plane	Relevance-100/ Relevance Center-Fine / Smoothing -High	Sizing (rot - all body) - 3mm	smooth Transition - 20 Layers
1 - Without End Plane	Relevance-100/ Relevance Center-Fine / Smoothing -High	Sizing (rot - all body) - 5mm	smooth Transition - 20 Layers
1 - With End Plane	Relevance-100/ Relevance Center-Fine / Smoothing -High	Sizing (rot - all body) - 3mm	smooth Transition - 20 Layers
1.25 - Without End Plane	Relevance-100/ Relevance Center-Fine / Smoothing -High	Sizing (rot - all body) - 5mm	smooth Transition - 20 Layers
1.25 - With End Plane	Relevance-100/ Relevance Center-Fine / Smoothing -High	Sizing (rot - all body) - 3mm	smooth Transition - 20 Layers
1.5 - Without End Plane	Relevance-100/ Relevance Center-Fine / Smoothing -High	Sizing (rot - all body) - 5mm	smooth Transition - 20 Layers
1.5 - With End Plane	Relevance-100/ Relevance Center-Fine / Smoothing -High	Sizing (rot - all body) - 3mm	smooth Transition - 20 Layers

Table 5. Mesh quality values of rotors (Ansys according to fluent guide) – Without end plane.

Quality Values						
Element Quality						
Aspect Ratio (H/ D _{rotor})	Minimum	Maximum Value	Average Value	Deflection	Node	Element
0.75	0.0013508	1	0.6152	0.35357	400601	1416339
1	0.0030653	1	0.63781	0.34275	450761	1647751
1.25	0.0028844	1	0.63428	0.34441	462741	1681616
1.5	0.0029779	1	0.63054	0.34577	475660	1718988
Orthogonal Quality						
Aspect ratio (H/ D _{rotor})	Minimum	Maximum Value	Average Value	Deflection	Node	Element
0.75	0.010355	0.99973	0.85181	0.14358	400601	1416339
1	0.019847	0.99956	0.85458	0.13205	450761	1647751
1.25	0.020251	0.99958	0.85402	0.113199	462741	1681616
1.5	0.019359	0.99941	0.85333	0.13174	475660	1718988
Skewness						
Aspect Ratio (H/ D _{rotor})	Minimum	Maximum Value	Average Value	Deflection	Node	Element
0.75	3.9961E-08	0.8496	0.22464	0.13629	400601	1416339
1	2.6512E-09	0.83892	0.22514	0.13286	450761	1647751
1.25	5.88E-08	0.84225	0.22599	0.13159	462741	1681616
1.5	1.9015E-08	0.84561	0.22674	0.13118	475660	1718988

Table 6. Mesh quality values of rotors (Ansys according to the fluent guide) - With end plane.

Quality Values						
Element Quality						
Aspect Ratio (H/ D _{rotor})	Minimum	Maximum Value	Average Value	Deflection	Node	Element
0.75	0.00056418	1	0.64077	0.34183	1416700	5227374
1	0.0013066	1	0.65871	0.33334	1350220	5142735
1.25	0.0014164	1	0.67105	0.34441	1306853	5086620
1.5	0.00070041	1	0.67731	0.32353	1289496	5080500
Orthogonal Quality						
Aspect Ratio (H/ D _{rotor})	Minimum	Maximum Value	Average Value	Deflection	Node	Element
0.75	0.014166	0.9999	0.87239	0.12019	1416700	5227374
1	0.01449	0.99992	0.87121	0.11812	1350220	5142735
1.25	0.016188	0.99992	0.87024	0.11764	1306853	5086620
1.5	0.014206	0.99975	0.86907	0.11738	1289496	5080500
Skewness						
Aspect Ratio (H/ D _{rotor})	Minimum	Maximum Value	Average Value	Deflection	Node	Element
0.75	2.0853E-09	one	0.20899	0.13154	1416700	5227374
1	2.0851E-09	0.93733	0.20865	0.13017	1350220	5142735
1.25	2.1347E-09	0.93003	0.20886	0.12915	1306853	5086620
1.5	2.1311E-09	0.92284	0.21037	0.12849	1289496	5080500

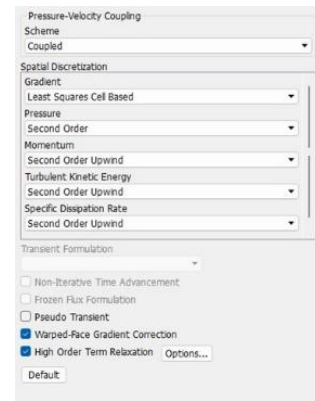


Figure 13. Solution method and parameters to be used in analysis

In the analysis program, the solution methods were applied as shown in the above figure in all of the analyzes performed as steady on the flow images. In the analyzes performed in steady-state, the analysis was completed with 2000 iterations.

As mentioned before, the inconsistency of numerical analyzes with experimental analyzes is not due to the input values written in the program, but to the appropriate mesh number and the inability to reach a solution independent of this mesh number. The data obtained from the numerical analyzes were used only to compare the data obtained from the experimental analyzes with each other.

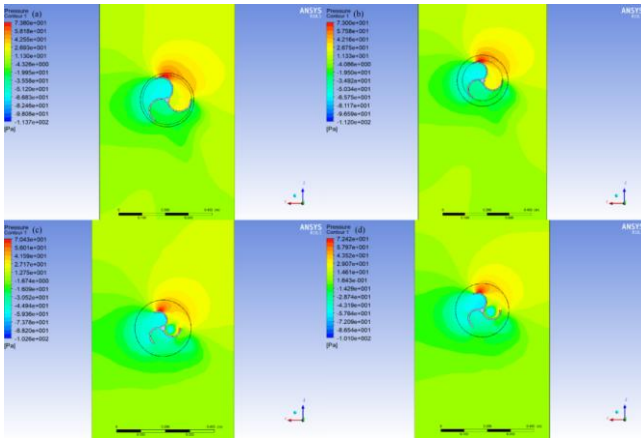


Figure 14. Pressure distribution on XZ plane of rotors with aspect ratio of a-0.75 (With end plane and $n = 546$ rpm), b-1 (With end plane and $n = 516$ rpm), c-1.5 (Without end plate and $n = 534$ rpm) and d-1.25 (Without end plate and $n = 558$ rpm)

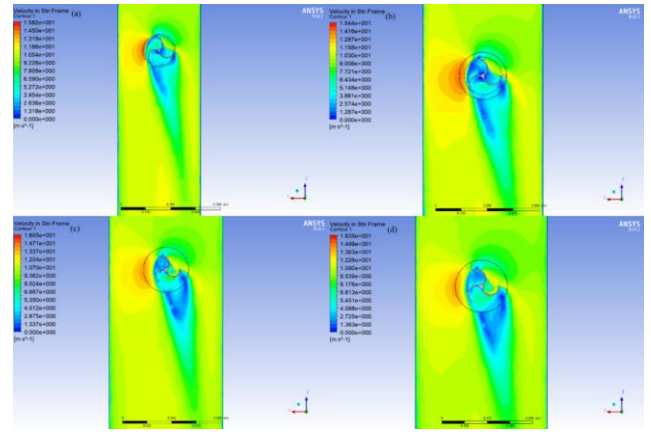


Figure 16. Velocity distribution on the XZ plane of rotors with aspect ratio of a-0.75 (With end plane and $n = 546$ rpm), b-1 (With End Plane and $n = 516$ rpm), c-1.5 (Without end plate and $n = 534$ rpm) and d-1.25 (Without end plate and $n = 558$ rpm)

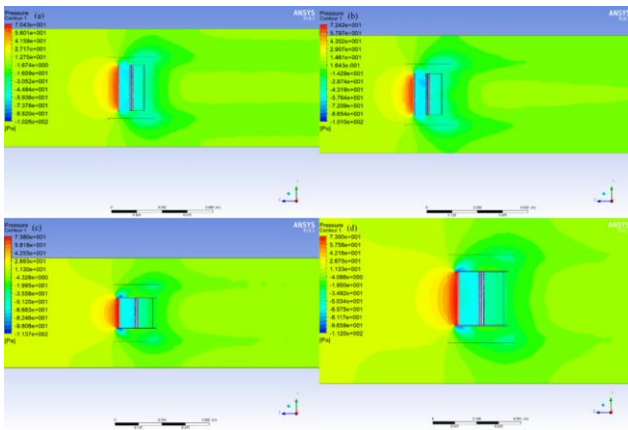


Figure 15. Pressure distribution on the YZ plane of rotors with aspect ratio of a-0.75 (With end plane and $n = 546$ rpm), b-1 (With End Plane and $n = 516$ rpm), c-1.5 (Without end plate and $n = 534$ rpm) and d-1.25 (Without end plate and $n = 558$ rpm)

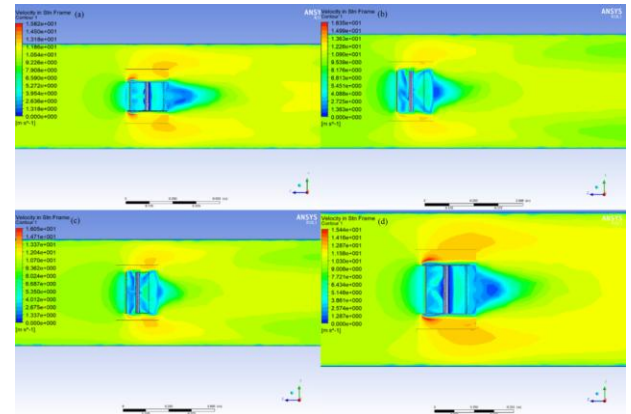


Figure 17. Speed distribution on the YZ Plane of rotors with aspect ratio of a-0.75 (With end plane and $n = 546$ rpm), b-1 (With End Plane and $n = 516$ rpm), c-1.5 (Without end plate and $n = 534$ rpm) and d-1.25 (Without end plate and $n = 558$ rpm)

The representations in the XZ and YZ planes in figures 14 and 15, with the angular velocity values corresponding to the values in the maximum power coefficient obtained from the experimental analysis of the rotors with aspect ratio 0.75 (without end plate), 1 (without end plate), 1.25 (with end plate) and 1.5 (with end plate). The pressure distribution obtained from the numerical analyzes made is observed. As observed, negative pressure was observed in the rotors without end plate. However, this was not observed in rotors with end plates. This is also observed in the case of the rotors with and without the end plate, which have the same aspect ratio. In other words, in the case of uncapped rotors with end plates, this negative pressure disappears and it is observed that the torque values increase when compared with the ensuing torque increase at the same angular speeds. This is basically what is meant here.

The representations in the XZ and YZ planes in figures 16 and 17, with the angular velocity values corresponding to the values in the maximum power coefficient obtained from the experimental analysis of the rotors with aspect ratio 1.25 (without end plate), 1.5 (without end plate), 1 (with end plate) and 0.75 (with end plate). The velocity distribution obtained from the numerical analyzes made is observed. As observed, speed drops due to negative pressure were observed in rotors without end plate. However, this was not observed in rotors with end plates. This is also observed in the case of the rotors with and without the end plate, which have the same aspect ratio. In other words, when the rotors without end plate are end plates, this negative pressure disappears and it is observed that the torque values increase when compared with the subsequent torque increase at the same angular speeds. It can be said that a stable flow opportunity is also offered

Table 7. Torque values from analyzes

Name	Experimental		Numerical		Relative Error (%)
	n (rpm)	T (Nm)	n (rpm)	T (Nm)	
With End Plate -0.75-Rotor	546	0.0154	546	0.0249	61,6883
With End Plate -1-Rotor	516	0.0158	516	0.0208	31,6456
Without End Plate -1.25-Rotor	558	0.011	558	0.0164	49,0909
Without End Plate -1.5-Rotor	534	0.0092	534	0.0104	13.0435

Table 7 above shows the rotational numbers of the first two rotors with the maximum power coefficients according to the results of the experimental analyzes of the rotors (with/without end plate) and the experimental and numerical values of the torque values according to these revolutions. In addition, the pressure and velocity indications of the analyzes made for flow monitoring against these numerical values are shown above. Although the numerical data in Table 7 do not agree with the experimental data, the images made support the inferences made from the experimental analysis. In addition to this, additional numerical analyzes (steady) were made to compare the rotors with and without the end plate themselves. In addition to displaying the pressure and velocity distributions from these analyzes, vectorial velocity distributions were taken to examine how the air behaves during the movement of the rotors. In Table 7, in order to reduce the difference between the torque values obtained from numerical analyzes and experimental analyzes, even though it is tried to approach realistic results by entering the roughness values in the wall definition in the rotor part in the numerical analysis, there is not much difference in the results obtained.

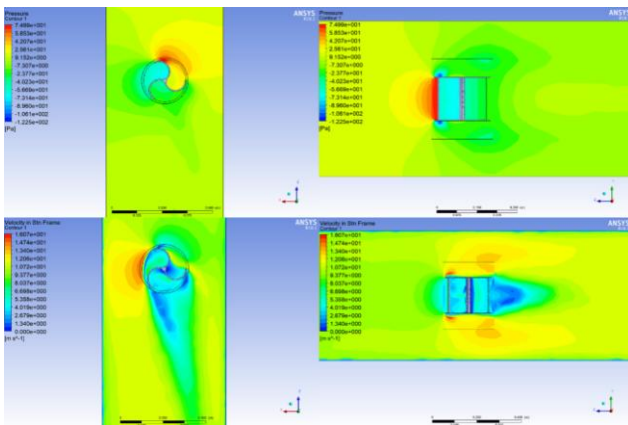


Figure 18. Pressure and velocity distribution on XZ and YZ planes of a rotor with aspect ratio of 0.75 (With end plate) (n = 588 rpm)

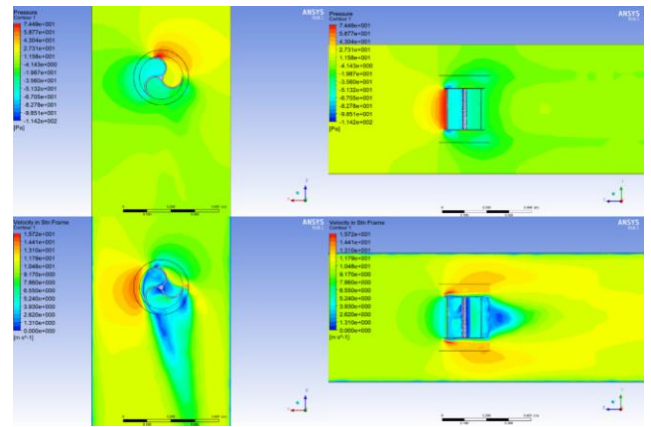


Figure 19. Pressure and velocity distribution on XZ and YZ planes of a rotor with aspect ratio of 1 (With end plate) (n = 588 rpm)

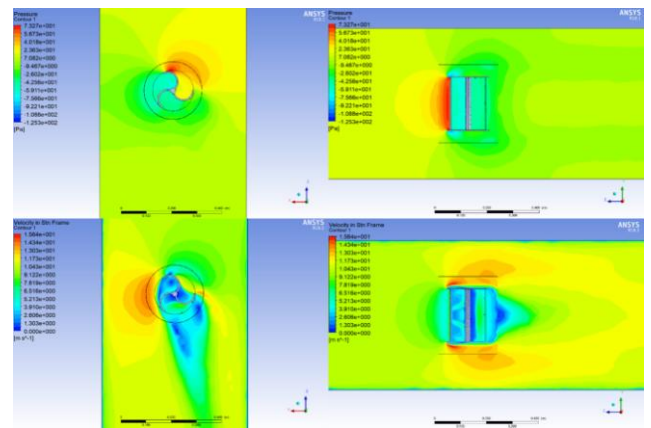


Figure 20. Pressure and velocity distribution on XZ and YZ planes of a rotor with aspect ratio of 1.25 (With end plate) (n = 588 rpm)

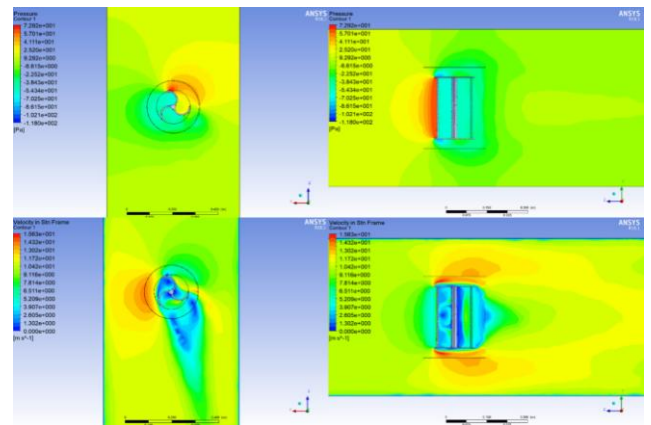


Figure 21. Pressure and velocity distribution on XZ and YZ planes of a rotor with aspect ratio of 1.5 (With end plate) (n = 588 rpm)

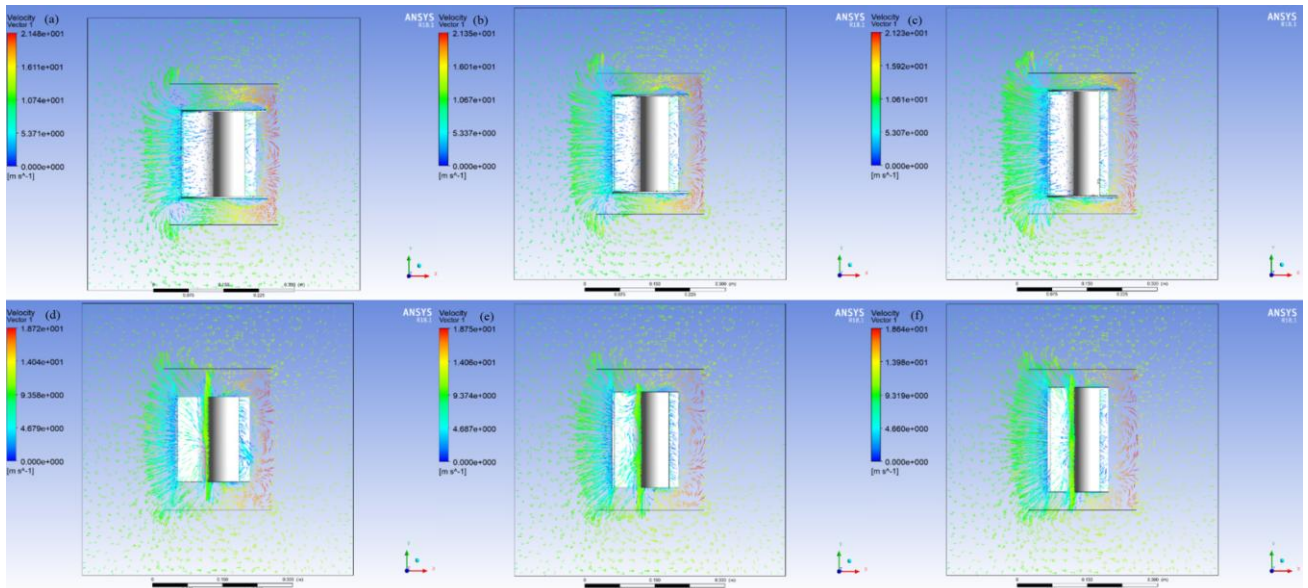


Figure 22. Vectorial velocity distribution on XY plane of rotors with aspect ratio of a-1 (With end plate and $n = 588$ rpm), b- 1.25 (With end plate and $n = 588$ rpm), c- 1.5 (With end plate and $n = 588$ rpm), d- 1 (Without end plate and $n = 420$ rpm), e-1.25 (Without end plate and $n = 420$ rpm) and f- 1.5 (Without end plate and $n = 420$ rpm).

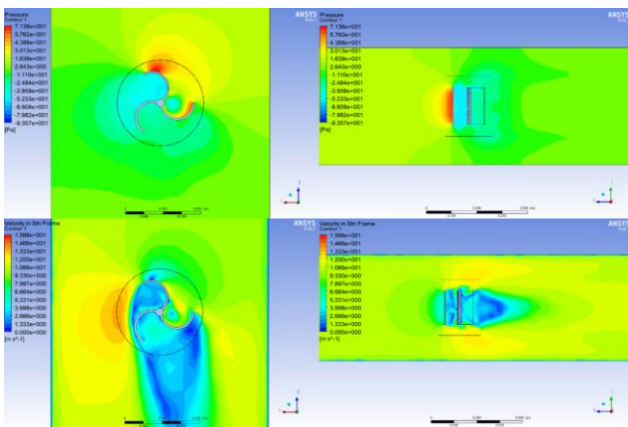


Figure 23. Pressure and velocity distribution on XZ and YZ planes of a rotor with aspect ratio of 1 (Without end plate) ($n = 420$ rpm)

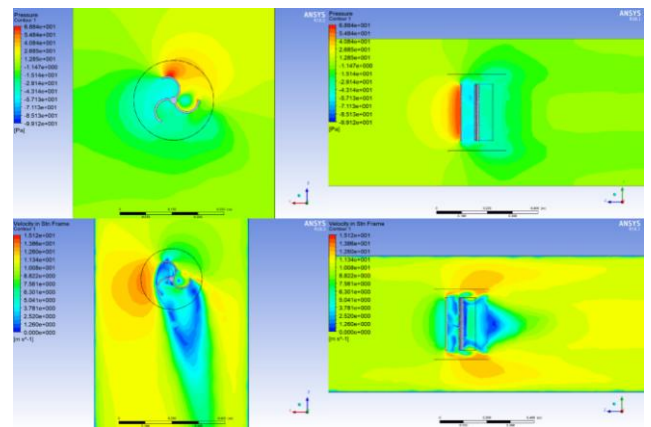


Figure 25. Pressure and velocity distribution on XZ and YZ planes of a rotor with aspect ratio of 1.5 (Without end plate) ($n = 420$ rpm)

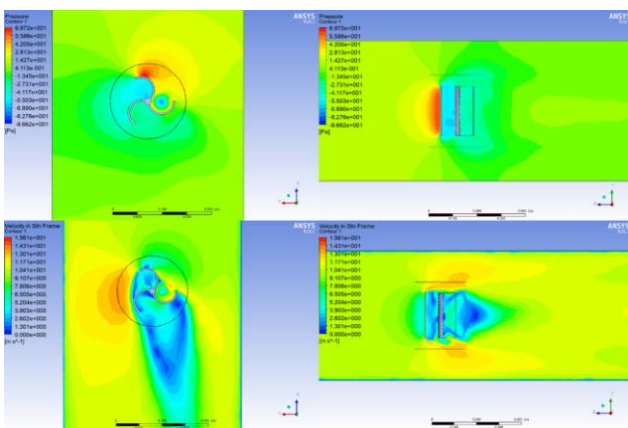


Figure 24. Pressure and velocity distribution on XZ and YZ planes of a rotor with aspect ratio of 1.25 (Without end plate) ($n = 420$ rpm)

4. DISCUSSION AND CONCLUSION

4.1 Discussion

The pressure-velocity distributions of capped rotors at 588rpm (fig. 18-21) and the pressure-velocity distribution of uncapped rotors at 420rpm (fig. 23-25) are shown above. While the aspect ratios of 0.75, 1, 1.25, and 1.5 were examined respectively in capped cases, rotors with 1, 1.25, and 1.5 ratios were examined in caseless ones, respectively. The rotor with end plates aspect ratio of 0.75 was not included in the comparison since the desired rpm speeds were not achieved experimentally. Looking at the inside of the blade that meets the air of the covered rotors, it is smooth and the maximum pressure value of 0.75 is read, respectively, and the smallest pressure value is seen at 1.5 (Figures 18-21). Although the values shown in the pressure distribution seem close to each other, they differ in terms of the penetration of the pressures and support the experimental studies. Negative pressure was observed

inside the blade that meets the air in the flow imaging of the rotors without end plate (Figures 23-25). The reason for this is that the air cannot be trapped inside the blade in rotors without end plate. In addition, the pressure drops due to the eddy flow in the blade and around the rotor caused a decrease in the torque and power coefficient. The vectorial movements of the pair shown in Figures 22, also support this situation. In the experimental study, it has been observed that 1.25 has higher efficiency than 1.5 in the rotors without end plate. The reason for this is that in the numerical study, higher negative pressure was observed in the rotor blade with a ratio of 1.5, seen in figures 23 and 24, compared to 1.25.

In general, when the rotors are compared with and without the end plate, according to the results obtained from the experimental analysis, it has been observed that the torque (power) produced in the closed cases at the same rpm values is higher than the torque produced without the end plate. Due to the numerical imaging made earlier, the efficiency decrease due to the negative pressure in the capless ones was not observed in the capped state, and it caused an abnormal increase in efficiency in some rotors (example 0.75).

4.2 Conclusion and Suggestions

According to the results obtained from the analysis, rotors with small aspect ratios in the case of the rotors without end plate have lower power coefficients and their overall performances have increased with the increase in aspect ratios. It has been concluded that the pressure values encountered by the rotors are directly related to the power coefficients they produce. However, the opposite effect was observed this time in the analysis of the rotors with the end plate. Here, the low aspect ratios caused the power coefficients to increase more than the others. The numerical analyzes performed for flow monitoring to compare the rotors with each other in both without the end plate and with the end plate states at equal revolutions also agree with the results obtained from the experimental analyzes.

Acknowledgments

Who provided to us with all kinds of help and sacrifices during our work, we would like to thank my esteemed teachers Prof. Dr. Selahaddin Orhan AKANSU and Prof. Dr. Sebahattin ÜNALAN.

REFERENCES

[1] S. R. Paramatia, U. Shahzad and B. Doğan, The role of environmental technology for energy demand and energy efficiency: Evidence from OECD countries, *Renewable*

and Sustainable Energy Reviews, vol. 153, pp. 111735, 2022.

[2] O. Edenhofer, et al., *Renewable energy sources and climate change mitigation: Special report of the intergovernmental panel on climate change*, Cambridge University Press, 2011.

[3] B. Metz, O. R. Davidson, P. R. Bosch, R. Dave, and L. A. Meyer, *IPCC Climate Change 2007: Mitigation of Climate Change*, Cambridge University Press, 2007.

[4] M. B. Akkuş, Z. Haksever and S. Teksin, *Experimental and Numerical Analysis of Savonius Wind Turbine with End Plate on Various Types*, *Energy, Environment and Storage*, vol. 2, pp. 61-70, 2022.

[5] M. H. Ali, *Experimental comparison study for Savonius wind turbine of two & three blades at low wind speed*, *International Journal of Modern Engineering Research*, vol. 3, pp. 2978-2986, 2013.

[6] B. D. Altan, G. Altan and V. Kovan, *Investigation of 3D printed Savonius rotor performance*, *Renewable Energy*, vol. 99, pp. 584-591, 2016.

[7] Z. Zhao, et al., "Research on the improvement of the performance of Savonius rotor based on numerical study," *2009 International Conference on Sustainable Power Generation and Supply*, IEEE, 2009.

[8] V. Kharade and K. Jagtap, *A Review Study on Vertical axis Wind Turbines (lift and drag type) for Optimizing the Aerodynamic and Structural Performance*, *IOSR Journal of Engineering*, vol. 3, pp. 61-65, 2019.

[9] M. Zemamou, M. Aggour and A. Toumi, *Review of savonius wind turbine design and performance*, *Energy Procedia*, vol. 141, pp. 383-288, 2017.

[10] İ. Gül and A. Kolip, *Parça Kanatlı Savonius Rüzgâr Türbin Performansının İncelenmesi*, *El-Cezerî Journal of Science and Engineering*, vol. 5, pp. 816-827, 2018.

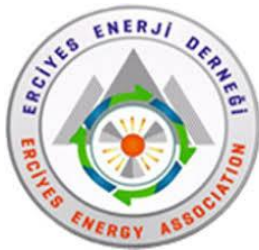
[11] K. S. Jeon, J. I. Jeong, J. K. Pan, and K. W. Ryu, *Effects of end plates with various shapes and sizes on helical Savonius wind turbines*. *Renewable energy*, vol. 79, pp. 167-176, 2015.

[12] C. Schubert, M. C. Van Langeveld and L. A. Donoso, *Innovations in 3D printing: a 3D overview from optics to organs*, *British Journal of Ophthalmology*, vol. 98, pp. 159-161, 2014.

[13] İ. Yılmaz, Ö. Çam, M. Taştan and A. Karcı, *Experimental Investigation of Aerodynamic Performance of Different Wind Turbine Airfoils*, *Journal of Polytechnic*, vol. 19, pp. 577-584, 2016.

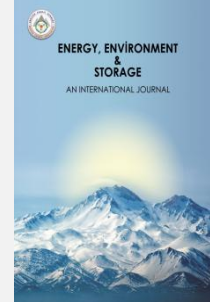
[14] ANSYS Fluent Theory Guide 15.0, ANSYS, 2013.

[15] M. A.A. Nawar, et al. *On the enhancement of Savonius Bach-type rotor performance by studying the optimum stator configuration*, *Ocean Engineering*, vol. 217, pp. 107954, 2020.



Energy, Environment and Storage

JournalHomepage: www.enenstrg.com



Phase Change Materials for Energy Efficiency in Building Components – Overview

Rachit Agarwal¹, Pradeep Rawat¹, Devendra Rai², Humaira Athar¹, Srinivasarao Naik B^{1*}

¹IBM Group, CSIR-Central Building Research Institute, Roorkee

²Department of Chemical Engineering, Indian Institute of Technology Roorkee

ABSTRACT: Energy demand in the building particularly in summer during peak hours due to outdoor climate and lack of sufficient high thermal mass construction materials. Advanced materials are required to reduce the recurring energy demand of buildings. This peak hour energy demand can be significantly reduced by using phase change materials (PCM). These PCMs are being incorporated into building components/ products in various ways. In this overview, the recent advances in the field of using different types of PCMs, parameters to be considered for building components, encapsulation of PCMs and influence of PCMs on thermal and mechanical properties of construction materials are briefly discussed. Importantly, behaviour of MPCM in building components is concisely elaborated in effective way.

Keywords: Energy demand, Phase change material, Thermal mass, Encapsulated phase change material

Doi: <https://doi.org/10.52924/ADSZ4322>

1. INTRODUCTION

In India currently energy consumption in residential and commercial building accounts for 30% of total energy use and this consumption is raising 8% annually. Energy consumption in buildings is dependent on outdoor climate, building construction materials, naturally ventilated or air-conditioned, occupancy hours, thermal comfort expectations of occupants, office equipment and home appliances [1]. Energy demand in the buildings can be accomplished either by using sensible heat or latent heat materials. Sensible heat materials have been used for centuries by builders to store/ release passively thermal energy, but larger volume of material is required in comparison of latent heat i.e. phase change materials (PCMs) [2]. PCMs are commercially available in the market from -3 °C to 850 °C [3]. Day time, when the temperature is above the melting point, the PCM absorbs heat during the material changes phase from solid to liquid. At night, when the temperature is below the melting point, the PCM desorbs heat to ambient, during the material changes phase from liquid to solid. The PCMs are being successfully used as energy storage devices in heat pumps, solar engineering, space craft etc. The use of PCMs into the buildings is the incorporation of PCMs into the building components as these PCMs undergo phase transformation process and therefore, suffer from the problems of leakages. Most of the researchers have been working in the direction of micro/nano-PCM capsules to overcome these difficulties [4]. Particularly in building, these PCMs are integrating in walls, mortar,

concrete and paints for delay the heat transfer, peak load shifting, reduction of temperature fluctuation and enhancement of thermal properties of cementitious materials. In this report, information provided about PCMs which were used in the buildings by possible ways.

The importance of this study is highlighted for a better understanding of how phase change materials affect cementitious materials, as well as the mechanisms that cause mechanical qualities to be reduced and thermal properties to be increased. In addition, what factors need to be taken into account and offered should be evaluated before incorporating into any system.

2. HOW TO SELECT THE PCMS?

Before incorporating into buildings or thermal energy storage systems, PCMs should be selected based on thermal, physical, kinetic and chemical properties

2.1 Thermal point of view:

PCM Thermal conductivity should be either high or low, which depends on applications (buildings/thermal energy storage systems), thermal stability, and a high heat of fusion (H.F kJ/kg) of PCM should be high.

2.2 Physical point of view:

High energy density during phase transition and small volume change.

2.3 Kinetic Point of view:

No super cooling during PCM changes from liquid to solid.

2.4 Chemical point of view:

Along-term chemical stability of PCM (functional contained in PCMs should not be react with other materials), non-toxicity and no fire hazard.

2.5 Economic Point of view:Cost effective and PCM should be easily available.

3. TYPES OF PCMS

Phase change materials are divided into three categories (i) Organic (ii) Inorganic (iii) Eutectic mixture

3.1 Organic PCMs

The organic phase change compounds are chemically stable, no super cooling, non-corrosive and nontoxic. Organic PCMs are subdivided in two groups (i) Paraffins (ii) Non paraffins. Paraffins are chemically inert, have low thermal conductivity and large volume change. The non-paraffins such as fatty acids have high heat of fusion than paraffins and have small volume change.

3.2 Inorganic PCMs

Inorganic PCMs have high heat of fusion, good thermal conductivity, are cheap and nonflammable. Most of them are corrosive to metals. Most inorganic PCMs are hydrated salt. Hydrated salts have a high energy density and high thermal conductivity. Disadvantage is that undergoes super cooling.

3.3 Eutectic Mixture

Eutectic mixture is a mixing of more than one PCM material. Eutectic mixtures have sharp melting point and energy density is slightly higher than that of organic PCMs. Eutectics are divided in three groups (i) Organic – Organic (ii) Inorganic – Inorganic (iii) Organic – Inorganic [1, 5]. The desired temperature range of eutectic mixture can be designed according to Schroder’s equation (1) [6]

$$\ln x_A = \frac{\Delta H_A}{R} \left(\frac{1}{T} - \frac{1}{T_f} \right) \quad (1)$$

where x_A and ΔH_A are the molar fraction and latent heat of fusion kJ/kg of compound A, respectively. T and T_f are the melting temperature °C of the mixture and compound A. R is gas factor 0.8314 kJ/ K. mol.

3.4 Commercial availability of PCMs

In the market, the companies/industries such as BASF, Microtek and Rubitherm are commercializing the encapsulated PCMs (EPCMs/MPCMs) with the name of DS5001X, RT 5, and RT 25 etc. within temperature range of below ambient to above 100°C (Table 1)[3, 7-11].

Table 1 Commercially Available MPCM companies

Company Name	Commercial name of PCM	Website
Microteck BASF, Dayton	Micronal and MPCM	Product Data Sheets - Microtek Labs[11]
RAL quality association PCM, Germany	Rubitherm GmbH	rubitherm technologies gmbh-PCM-Phase change Material (pcm-ral.org)[10]
PCM energy, UK	-----	PCM Products Phase Energy Ltd (phase-energy.com)[12]
Climator, Sweden	ClimSel	PCM-ClimSel (climator.com)[9]
Thermofin	-----	CRISTOPIA : Thermal energy storage solution - THERMOFIN[7]

4. INCORPORATION OF PHASE CHANGE MATERIALS INTO BUILDING COMPONENTS

The PCMs are incorporated in construction materials by, immersion and encapsulation methods

4.1 Immersion

In the immersion technique, the construction elements (concrete, brick blocks, and wallboards), which are dipped into the liquid PCM (at above melting point), absorbs the PCM in the pores contained in the building materials by capillary action under the vacuum pressure Fig. 1[13]. It is reported that PCM may leak [14-16] especially after subjected to many thermal cycles. Also, it may affect the mechanical and durability properties of the construction elements. These essentials points need to be considered for building components.

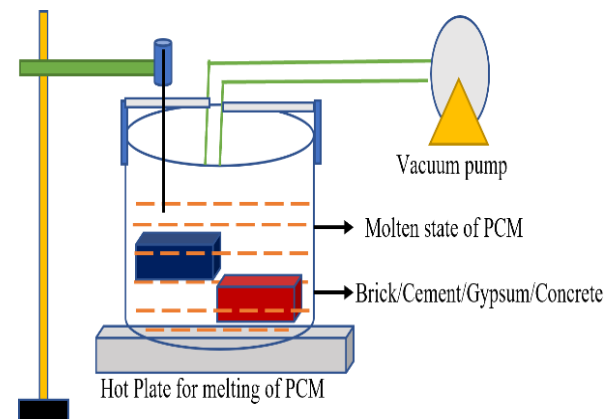


Fig.1 Immersion method

4.2. Encapsulation

In this technique, PCMs are encapsulated in either polymer shell or inorganic shell before incorporation into construction materials. PCM encapsulation should (a) meet the requirement of strength, durability, thermal stability of polymer/shell (b) it protects the PCM as a barrier, from destructive interactions with the surrounding (c) have enhance surface area for heat transfer. There are two types of encapsulation methods one is microencapsulation, and another is macro-encapsulation [3, 17, 18].

4.2.1. Microencapsulation

Encapsulation is a tiny particle where in PCM as a core material which is surrounded by polymer as a shell (Fig.2)[17]. The phase change temperatures in between ambient to 80 °C can be prepared with this technique. There are two methods of micro-encapsulation: Physical and Chemical methods [19]. The physical method includes Fluidized bed process and spray drying (SD) while the chemical methods include In Situ Polymerization (ISP), Complex Coacervation (CC), Phase Separation (PS) and Suspension- Polymerization (SP). Preparation methods of encapsulated techniques and PCMs by literature given in Table 2[20]. Borreguero et al. (2011)[21] developed encapsulations of paraffin (RT27) with and without carbon nanofibers (CNFs) utilising the spray process and a coated shell made of polyethylene-ethylvinylcetate (LDPE-EVA). The smooth, sphere-shaped microcapsules have a particle size range of 0.1 to 5.0 m. Latent heat of fusion (LHF) and

encapsulation efficiency (EE) were 80% and 92 J/g, respectively (Fei et al., 2008) [22]. Using sophisticated coacervation, Xiao et al. (2014) [23] created microcapsules with a lavender oil core and a gelatin exterior, as well as gum. On the appearance, average particle size, yield, and EE, several values including pH value, C/S ratio, shell concentration, agitator speed, cross-linkers, and homogenization rate were studied. pH 3.5, C/S 3:2, 1% shell concentration, 450 rpm speed, and glutaraldehyde as a cross-linker were the ideal conditions for creating the microcapsules. The EF, loading capacity, and yield were each 65.8 1.0%, 66.0 0.3%, and 61.3 7.0%, respectively. Phase change material (PCM) microcapsules were created by Devenci and Basal in 2009 [24] using n-Eicosan as the core and silk fibroin (SF) and chitosan (CHI) as the shell. For the coacervation procedure used by Butstraen and Salaün (2014)[25] to encapsulate coloured oil, the following parameters were optimised: pH 3.6, weight ratio of chitosan to acacia gum combination of 0.25, C/S 0.1, and emulsion period of 15 min at 11,000 rpm. In-situ polymerization was used by Hong and Park (1999) [26] to successfully create microcapsules using aromatic Margin oil as the core material and melamine formaldehyde as the shell material. They found that the microencapsulation effectiveness was about 87% and that the particle size was below 10 µm. The capsules were created by Liang et al. (2015) [27] using n-octadecane and SiO₂, with a latent heat of silica PCM of 109.5 kJ/kg. Tris (hydroxyethyl) methyl amino methane, SiO₂, and its latent heat of about 146 kJ/kg were combined to create capsules by Wu et al. in 2015[28].

Table2. Micro-encapsulation Techniques

Method	Particle size (µm)
Spray Drying	0.1 - 5000
Coacervation	2-1200
Sol-Gel	0.2 to 20
Interfacial Polymerization	0.5 - 1000
Suspension Polymerization	2-2000
In situ-Polymerization	5-300 nm

The most used polymers are Melamine – formaldehyde (MF), Urea Formaldehyde (UF), Poly styrene (PS), Poly methyl methacrylate (PMME), Melamine-urea formaldehyde (MUF), Silica oxide (SiO₂), Titanium oxide (TiO₂) etc.

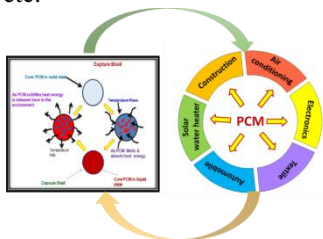


Fig.2 Behaviour of MPCM into different applications

4.2.2 Macro-encapsulation

In this technique, a significant quantity of PCM can be packed in a container such as tubes, spheres and panels for subsequent used in construction elements [29]. The macro-encapsulation is available in various configurations like flat plate, cylinder shell, tube and spherical (Fig.3)Also, it may affect the mechanical and durability properties of the construction elements. Shin et al.2015 [30], sodium acetate trihydrate containing 2.5 wt% expanded graphite had a thermal conductivity of 1.85 W m⁻¹ K⁻¹, which was much greater than Ffor pure samples, 0.3 W m⁻¹ K⁻¹.

According to Jin et al. [31], the best place for PCM pouch systems was 1/5 L away from the internal surface of walls (where L was the wall thickness). According to Fang [32], PCM tube systems positioned at a distance of (3/16)L from the inner surface would result in significant peak reductions. The various ideal positions discovered through these investigations suggest that various factors can affect such a site. To learn more about the impact of various variables, including wall orientations, PCM system thicknesses, and PCM thermal characteristics, some researches were carried out.

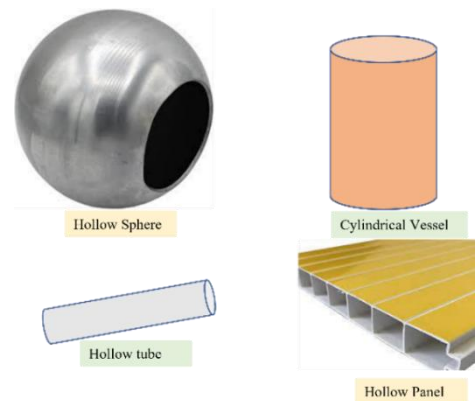


Fig 3Macro-encapsulation materials for PCM

4.2.3Shape-stabilized PCM

In this technique, shape stabilization supports polymers such as high- density polyethylene (HDPE), Styrene and Different molecular weight of Polymers etc. The PCM and supporting material is melted and mixed with each other at high temperature and poured into ant three-dimensional mould.The supporting material is cooled to below the glass transition temperature until it becomes solid (Fig.4). The mass of the PCM can be incorporate up to 80%. These panels can be used as retrofitted to the building [29, 33, 34].

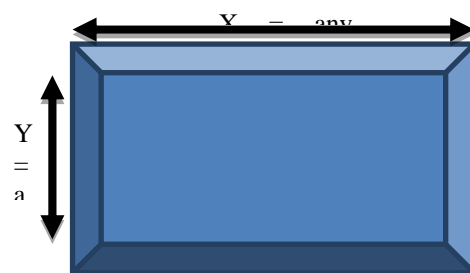


Fig 4.Shape stabilized PCM

Shape-stabilized PCM is being prepared by researchers according to their specifications (Fig.4). There are certain key dimensions that have not yet been investigated.

5. EFFECTS OF PCM ON THERMAL PROPERTIES OF BUILDING COMPONENTS

Thermal conductivity and specific heat are considering parameters for building component Micro-PCMs (melting point 23°C and heat fusion 100 kJ/kg) were mixed into the concrete. Thermal conductivity of the concrete is reduced as the percentage of PCM increased [35]. Eutectic mixture (melting point 21 °C and heat of fusion 126.652 kJ/kg) was incorporated into the gypsum by immersion method. Specific heat of phase change wallboards increased as compared with specific heat value of gypsum. According to research by Jayalath et al. (2016) [36], cementitious materials' thermal conductivity decreased by 37% when 5% microcapsules were added. Using 30% microcapsules, according to Xu and Li (2013)[37], increased thermal energy storage capacity by up to 5.438 kJ/kg. Gypsum thermal conductivity was examined by Jaworski and Abeid in 2011 [38]. 100% gypsum's thermal conductivity dropped from 0.35 W/m.K to 0.25 W/ (m.K). Gypsum's 0.1 W/m thermal conductivity was discovered at a PCM concentration of 30%. Using microcapsules, K. Zhang et al., 2020 [39] studied thermal conductivity. Gypsum materials' test results are 0.4707 W/ m.K, 0.3361 W/ m.K, 0.3011 W/ m.K, and 0.2537 W/ m.K, respectively, and these values correspond to microcapsule contents of 0, 5 wt.%, 10 wt.%, and 20 wt.%. It was thoroughly examined how M-PCM integration affected important characteristics as compressive strength, flexural strength, apparent density, porosity, and thermal behaviour. The apparent density and thermal conductivity of GC decrease with M-PCM incorporation (5 and 10%), but GC porosity rises with increasing M-PCM dose [40].

The thermal conductivity of incorporated MPCM into building materials were calculated theoretically by using the Maxwell eq. (2) which describes about the thermal conductivity of MPCM in building materials. Based on this model, the MPCM particles were unreacted with binding material and dispersion of MPCM in binding material homogeneously (Lecompte et al., 2015)[41].

$$k_{eff} = k_{bm} \frac{k_{MPCM} + 2k_{bm} + 2\theta(k_{MPCM} - k_{bm})}{k_{MPCM} + 2k_{bm} - \theta(k_{MPCM} - k_{bm})} \quad (2)$$

k_{eff} Effective thermal conductivity of incorporated MPCM into building material (W/m.K), k_{MPCM} thermal conductivity of MPCM (W/m.K), k_{CP} thermal conductivity of building material, θ is the volume fraction of MPCM. The specific heat of inclusion of MPCM building material was determined using the following eq. (3) and enthalpy of incorporated MPCM1 into the cement paste at phase transition temperature was determined using eq. (4) [42].

$$C_{peff} = (1 - \theta_{MPCM})C_{pbm} + \theta_{MPCM} C_{pMPCM} \quad (3)$$

$$H_{enthalpy \text{ of MPCM into bm}}$$

$$\text{at phase transition temperature} = \int_0^{T_{mp}} C_{peff} \Delta T \quad (4)$$

C_{peff} Specific heat of incorporated MPCM into building material(J/kg.K), C_{pcp} specific heat of building material (J/kg.K), C_{pMPCM} specific heat of MPCM (J/g.K), θ_{MPCM} volume fraction of MPCM. T_{mp} melting point of MPCM (K), H enthalpy of MPCM into building material (°C)

The thermal diffusivity of building material with MPCM was calculated using the following eq. (5)

$$\alpha = \frac{k}{\rho C_p} \quad (5)$$

Where, α is thermal diffusivity (m²/sec), ρ is the actual density of building material with MPCM samples and C_p specific heat of building material sample, J/kg.K.

6. MECHANICAL AND PHYSICAL PROPERTIES OF PCMS INTO BUILDING COMPONENT

Researchers have been studied mechanical properties of micro-PCMs into the concrete, cement, gypsum and brick. Compressive strength of building component decreased with addition of micro-PCMs. Compressive strength of concrete has been studied at 28 days by increasing micro-PCMs. Compressive strength of concrete significantly decreased while micro-PCMs dosage increased.

To enhance compressive strength of buildings components, nano materials are adding such as nano-SiO₂, TiO₂ and Carbon nano tubes (CNTs). Two kinds of dissimilar nano materials were used, one was nano silica (NS) which was in colloidal state and another one was nano titanium, (NT) in amorphous state, in mortars. The influence of nano materials NS and NT on the fresh and hardened state properties of these self-compacting mortars was studied. They concluded that the use of nano materials in repair and rehabilitation mortars has significant potential but still needs to be optimized [43]. Microcapsules were introduced to the cement-based system by Zhu et al. in 2021[44]. Porosity and density were assessed. As the microcapsule concentration was raised, the density decreased and the porosity rose. This effect can be explained by the fact that the LWA's pore structure is altered by the presence of microcapsules, which causes a drop in density as porosity rises. In place of PCM, Sukontasukkul et al. 2019 [45] investigated water absorption using light-weight aggregates (LWA). The density of the cement-based system (CBS) increases when LWA is substituted with PCM-LWA, and the absorption reduces. The density rises from 1747 kg/m³ to 1903 kg/m³ as the LWA is replaced by the PCM-LWA up to 100% by volume. The absorption decreases by 2.20-1.75% when the PCM-LWA totally replaces the LWA. In order to increase density and reduce absorption, denser aggregates (PCM-LWA) must be used in place of porous aggregates. Eddhahak-Ouni et al. (2014) [46] looked at the mechanical properties of PCC with micro-encapsulated paraffin PCM (Micronal DS 5001X). The samples containing 1%, 3%, and 5% microencapsulated PCM by volume, respectively, had compressive strengths that were 16%, 24%, and 32% lower than the reference sample (without PCM). A concrete tile system with microencapsulated paraffin was devised and tested by

Narain et al. in 2016 [47]. (Micronal DS 5008). Compressive strength was reduced by 25% when cement-based system (CBS) was used with 20% PCM per volume.

7. BASIC PARAMETERS FOR APPLICATION OF PCM IN DISTINGUISH APPLICATIONS

Based on overview, the following flowchart is drawn (Fig.5) for application of PCM in thermal energy storage system and building applications for reduction of energy demand [48]and it will be helpful to reduce burden on natural resources depletion

8.BEHAVIOUR OF MPCM IN BUILDING COMPONENTS

As the dosage of MPCM (shell : polymer) is increased, in cementitious material, thermal properties such as thermal conductivity and specific heat may be varied and also effects on mechanical properties such as compressive strength and flexural strength. In Fig.6, the briefly explained for above properties.

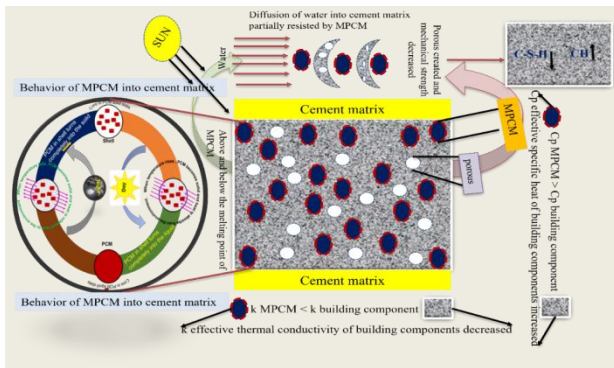


Fig.6 PCM plays in cementitious materials[49, 50]MPCM has a low thermal conductivity and high specific heat as compared to the building component. its effective total thermal conductivity is lowered than the control sample and higher specific heat. The mechanical properties are reduced.MPCM partially counterattacks the obligatory of water, therefore essential hydration products such as C-S-H is reduced as well as CH is increased. The C-S-H is principal product for improving the mechanical properties which can be improved by incorporating inorganic shell (Fig. 6).

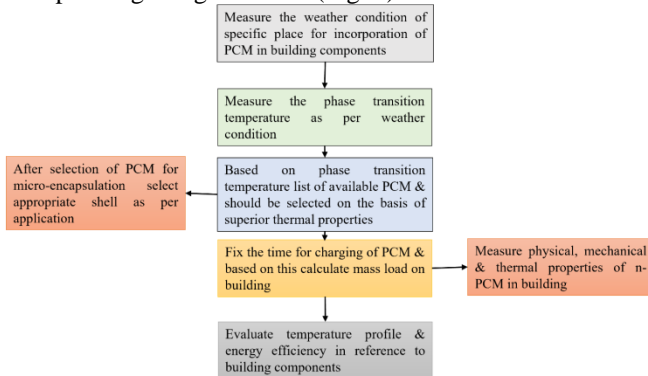


Fig.5 Flow chart for PCM design in different application

9. CONCLUSION

When selecting PCMs, their phase change temperature should be close to the average room temperature and comparison of thermal properties of PCMs at the average temperature, in that high latent heat of fusion, energy density must be select for the buildings. Other properties such as long-term thermal and chemical stability of PCMs considered. Successfully, polymers were used as shell to PCMs by different encapsulation methods, but their physic-thermal properties should be considered during selection of polymers. Shape stabilized PCM can be incorporate into interior of the building by retrofitting, it can enhance overall heat transfer coefficient. Thermal conductivity is decreasing, and specific heat is increasing, so PCMs may incorporate outside of building component. For this purpose, need to be analyze which temperature is suitable to the building component. Researchers have been studied mechanical properties of micro-PCMs into the concrete, cement, gypsum and brick. Whereas compressive strength is decreasing, while PCMs dosage increased. Compressive strength of PCMs building component can be enhance by adding nano materials

Acknowledgement

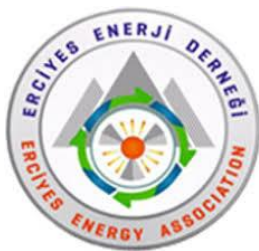
The authors are thankful to the Director, CSIR- CBRI for providing infrastructural facilities. The authors also acknowledge the financial support received from the Department of Science and Technology, Govt. of India through the project no.: GAP-0311.

REFERENCES

- [1] Global Buildings Performance Network, BUILDING POLICIES FOR CHANGE. www.gbpn.org, 2021, (Accessed 15 June 2022).
- [2] B. Zalba, J.M. Marin, L.F. Cabeza, H. Mehling, Review on thermal energy storage with phase change: materials, heat transfer analysis and applications, Applied thermal engineering, 23 (2003) 251-283.
- [3] F. Kuznik, D. David, K. Johannes, J.-J. Roux, A review on phase change materials integrated in building walls, Renewable and Sustainable Energy Reviews, 15 (2011) 379-391.
- [4] G. Fang, H. Li, F. Yang, X. Liu, S. Wu, Preparation and characterization of nano-encapsulated n-tetradecane as phase change material for thermal energy storage, Chemical Engineering Journal, 153 (2009) 217-221.
- [5] R. Baetens, B.P. Jelle, A. Gustavsen, Phase change materials for building applications: A state-of-the-art review, Energy and buildings, 42 (2010) 1361-1368.
- [6] L. Shilei, Z. Neng, F. Guohui, Eutectic mixtures of capric acid and lauric acid applied in building wallboards for heat energy storage, Energy and Buildings, 38 (2006) 708-711.
- [7] Cristopia. www.cristopia.com, (Accessed 10 May 2022).
- [8] Teapcm. www.teapcm.com, (Accessed 15 May 2022).
- [9] Climator. www.climator.com, (Accessed 22 May 2022).
- [10] Rubitherm. www.rubitherm.de, (Accessed 10 June 2022).
- [11] Basf. www.basf.com, (Accessed 19 May 2022).

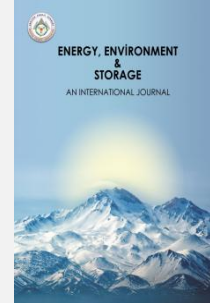
- [12] Phase Energy, Phase Change Materials (PCMs). <https://phase-energy.com/phase-change-materials-pcms/>, 2019, (Accessed 16 June 2022).
- [13] D.W. Hawes, D. Banu, D. Feldman, Latent heat storage in concrete, *Solar energy materials*, 19 (1989) 335-348.
- [14] D. Feldman, D. Banu, D. Hawes, E. Ghanbari, Obtaining an energy storing building material by direct incorporation of an organic phase change material in gypsum wallboard, *Solar energy materials*, 22 (1991) 231-242.
- [15] N. Soares, J.J. Costa, A.R. Gaspar, P. Santos, Review of passive PCM latent heat thermal energy storage systems towards buildings' energy efficiency, *Energy and buildings*, 59 (2013) 82-103.
- [16] D. Zhou, C.-Y. Zhao, Y. Tian, Review on thermal energy storage with phase change materials (PCMs) in building applications, *Applied energy*, 92 (2012) 593-605.
- [17] A. Waqas, Z.U. Din, Phase change material (PCM) storage for free cooling of buildings—A review, *Renewable and sustainable energy reviews*, 18 (2013) 607-625.
- [18] L.F. Cabeza, A. Castell, C.d. Barreneche, A. De Gracia, A.I. Fernández, Materials used as PCM in thermal energy storage in buildings: A review, *Renewable and Sustainable Energy Reviews*, 15 (2011) 1675-1695.
- [19] V. Tyagi, S. Kaushik, S. Tyagi, T. Akiyama, Development of phase change materials based microencapsulated technology for buildings: a review, *Renewable and sustainable energy reviews*, 15 (2011) 1373-1391.
- [20] Y. Fang, S. Kuang, X. Gao, Z. Zhang, Preparation and characterization of novel nanoencapsulated phase change materials, *Energy conversion and management*, 49 (2008) 3704-3707.
- [21] A.M. Borreguero, J.L. Valverde, J.F. Rodríguez, A.H. Barber, J.J. Cubillo, M. Carmona, Synthesis and characterization of microcapsules containing Rubitherm® RT27 obtained by spray drying, *Chemical Engineering Journal*, 166 (2011) 384-390.
- [22] B. Fei, H. Lu, K. Qi, H. Shi, T. Liu, X. Li, J.H. Xin, Multi-functional microcapsules produced by aerosol reaction, *Journal of aerosol science*, 39 (2008) 1089-1098.
- [23] Z. Xiao, W. Liu, G. Zhu, R. Zhou, Y. Niu, Production and characterization of multinuclear microcapsules encapsulating lavender oil by complex coacervation, *Flavour and fragrance journal*, 29 (2014) 166-172.
- [24] S.S. Deveci, G. Basal, Preparation of PCM microcapsules by complex coacervation of silk fibroin and chitosan, *Colloid and polymer science*, 287 (2009) 1455-1467.
- [25] C. Butstraen, F. Salaün, Preparation of microcapsules by complex coacervation of gum Arabic and chitosan, *Carbohydrate polymers*, 99 (2014) 608-616.
- [26] K. Hong, S. Park, Melamine resin microcapsules containing fragrant oil: synthesis and characterization, *Materials Chemistry and Physics*, 58 (1999) 128-131.
- [27] S. Liang, Q. Li, Y. Zhu, K. Chen, C. Tian, J. Wang, R. Bai, Nanoencapsulation of n-octadecane phase change material with silica shell through interfacial hydrolysis and polycondensation in miniemulsion, *Energy*, 93 (2015) 1684-1692.
- [28] C.-B. Wu, G. Wu, X. Yang, Y.-J. Liu, T. Liang, W.-F. Fu, M. Wang, H.-Z. Chen, Preparation of microencapsulated medium temperature phase change material of Tris (hydroxymethyl) methyl aminomethane@ SiO₂ with excellent cycling performance, *Applied Energy*, 154 (2015) 361-368.
- [29] P. Schossig, H.-M. Henning, S. Gschwander, T. Haussmann, Micro-encapsulated phase-change materials integrated into construction materials, *Solar energy materials and solar cells*, 89 (2005) 297-306.
- [30] H.K. Shin, M. Park, H.-Y. Kim, S.-J. Park, Thermal property and latent heat energy storage behavior of sodium acetate trihydrate composites containing expanded graphite and carboxymethyl cellulose for phase change materials, *Applied Thermal Engineering*, 75 (2015) 978-983.
- [31] X. Jin, M.A. Medina, X. Zhang, On the importance of the location of PCMs in building walls for enhanced thermal performance, *Applied energy*, 106 (2013) 72-78.
- [32] Y. Fang, A comprehensive study of phase change materials (PCMs) for building walls applications, Ph.D. Thesis, (University of Kansas), 2009
- [33] Y. Zhang, K. Lin, R. Yang, H. Di, Y. Jiang, Preparation, thermal performance and application of shape-stabilized PCM in energy efficient buildings, *Energy and buildings*, 38 (2006) 1262-1269.
- [34] A. Sari, Form-stable paraffin/high density polyethylene composites as solid-liquid phase change material for thermal energy storage: preparation and thermal properties, *Energy Conversion and Management*, 45 (2004) 2033-2042.
- [35] M. Hunger, A. Entrop, I. Mandilaras, H. Brouwers, M. Founti, The behavior of self-compacting concrete containing micro-encapsulated phase change materials, *Cement and Concrete Composites*, 31 (2009) 731-743.
- [36] A. Jayalath, R. San Nicolas, M. Sofi, R. Shanks, T. Ngo, L. Aye, P. Mendis, Properties of cementitious mortar and concrete containing micro-encapsulated phase change materials, *Construction and Building Materials*, 120 (2016) 408-417.
- [37] B. Xu, Z. Li, Paraffin/diatomite composite phase change material incorporated cement-based composite for thermal energy storage, *Applied energy*, 105 (2013) 229-237.
- [38] M. Jaworski, S. Abeid, Thermal conductivity of gypsum containing phase change material (PCM) for building applications, *Journal of Power Technologies*, 91 (2011) 49-53.
- [39] Y. Zhang, W. Tao, K. Wang, D. Li, Analysis of thermal properties of gypsum materials incorporated with microencapsulated phase change materials based on silica, *Renewable Energy*, 149 (2020) 400-408.
- [40] B. Srinivasaraonik, L.P. Singh, S. Sinha, I. Tyagi, A. Rawat, Studies on the mechanical properties and thermal behavior of microencapsulated eutectic mixture in gypsum composite board for thermal regulation in the

- buildings, *Journal of Building Engineering*, 31 (2020) 101400.
- [41] T. Lecompte, P. Le Bideau, P. Glouannec, D. Nortershauser, S. Le Masson, Mechanical and thermo-physical behaviour of concretes and mortars containing phase change material, *Energy and buildings*, 94 (2015) 52-60.
- [42] B. Srinivasaraonaik, S. Sinha, L.P. Singh, Studies on microstructural and thermo-physico properties of microencapsulated eutectic phase change material incorporated pure cement system, *Journal of Energy Storage*, 35 (2021) 102318.
- [43] S. Rao, P. Silva, J. De Brito, Experimental study of the mechanical properties and durability of self-compacting mortars with nano materials (SiO₂ and TiO₂), *Construction and Building Materials*, 96 (2015) 508-517.
- [44] L. Zhu, F. Dang, Y. Xue, W. Ding, K. Jiao, Experimental investigation of the thermal and mechanical properties of lightweight aggregate concrete mixed with microencapsulated phase change materials, *International Journal of Energy Research*, 45 (2021) 12864-12878.
- [45] P. Sukontasukkul, P. Uthaichotirat, T. Sangpet, K. Sisomphon, M. Newlands, A. Siripanichgorn, P. Chindapasirt, Thermal properties of lightweight concrete incorporating high contents of phase change materials, *Construction and Building Materials*, 207 (2019) 431-439.
- [46] A. Eddhahak-Ouni, S. Drissi, J. Colin, J. Neji, S. Care, Experimental and multi-scale analysis of the thermal properties of Portland cement concretes embedded with microencapsulated Phase Change Materials (PCMs), *Applied Thermal Engineering*, 64 (2014) 32-39.
- [47] J. Narain, W. Jin, M. Ghandehari, E. Wilke, N. Shukla, U. Berardi, T. El-Korchi, S. Van Dessel, Design and application of concrete tiles enhanced with microencapsulated phase-change material, *Journal of Architectural Engineering*, 22 (2016) 05015003.
- [48] B. Srinivasaraonaik, R. Agarwal, G. Mittal, L.P. Singh, Pre-Pilot scale Microencapsulation of phase change materials for thermal energy storage applications, *Energy, Environment and Storage*, 02 (2022) 41-53.
- [49] B. Srinivasaraonaik, S. Sinha, L.P. Singh, Phase Change Materials for Renewable Energy Storage Applications, *Management and Applications of Energy Storage Devices*, IntechOpen, 2021.
- [50] B. Srinivasaraonaik, Studies on Phase change materials incorporated building components, Ph.D. Thesis, (Indian Institute of Technology Roorkee (IITR), Roorkee), 2022



Energy, Environment and Storage

JournalHomepage: www.enenstrg.com



Hydroelectric Power Overview in 2021 of Turkey

Alaeddin Bobat

Kocaeli University Faculty of Agriculture Arslanbey Campus, 41285 Kartepe-KOCAELI
bobatus@gmail.com, ORCID: 0000-0003-4654-0208

ABSTRACT: Hydroelectric power together with other renewables already accounts for about 50% of electricity demand, and there is much additional potential for growth. Turkey is rapidly growing in terms of both its economy and its population. In parallel, its demand for energy, particularly for electricity, is increasing fast. Turkey's electric power demand has been developing steadily, averaging 8-10 % annual growth over the past 20 years. Turkey's hydraulic potential is 55,000 MW, and the share of hydraulic installed power has reached 31,647 MW from 11,175 MW in 2000 as of 31 December 2021. According to the Strategic Plan of the Ministry of Energy and Natural Resources for 2019-2023, while the total installed capacity will be about 32.9% in 2023, but this figure has already been reached. In cooperation with the public - private sector, 743 Hydroelectric Power Plants (public +private) with an installed capacity of 31,647 MW and a power generation potential of 108,932 GWh/year have been completed and put into service. Construction of those made by the public from these facilities is carried out by the DSI (State Hydraulic Works) and their operation is transferred to EUAS (Electricity Generation Corporation), while those made by the private sector, except for the EMRA license, other (water Use agreement, project, construction, water structures acceptance, etc.) operations are performed by DSI. From 743 facilities, 68 plants with an installed power of 13,766 MW with a power generation potential of 49 GWh/year by DSI, 675 plants with an installed power of 17,881 MW and a power generation potential of 60 GWh/year were built by the private sector and put into operation. This study aims to overview the status of hydropower in 2021 data of Turkey.

Keywords: Hydroelectric, Turkey, Status, Overview

Doi: <https://doi.org/10.52924/DFHK5620>

1. INTRODUCTION

Water is a valuable resource that is gradually decreasing. Population growth, industrialization and urbanization have led to a significant increase in water consumption in the world. Contrary to the general perception, Turkey is neither a country rich in freshwater resources nor the richest country in its region [1,2]. On the other hand, energy, especially renewables, means development, prosperity, stability and quality of life for every country. Turkey's electricity consumption increased by 7.7% compared to the year 2020 to 329.6 billion kWh in 2021, while electricity generation increased by 8.1% compared to the year 2020 to 331.5 billion kWh. The provision of energy on site, on time and at reasonable prices is indispensable for development. The development status of countries is gaining value with the presence of sustainable energy sources. Sustainable energy is to be able to meet the needs of today without jeopardizing the resources necessary to meet the needs of future generations [3-7].

In parallel with the significant development of the Turkish economy in recent years, it is observed that the consumption of electrical energy has also increased. The biggest obstacle to growth for the Turkish economy is the excessive need for import-dependent energy. Especially in recent years, with the widespread use of natural gas in Turkey, natural gas consumption has increased both for household and in industrial usages. Especially considering the decrease and disruptions in energy supply security after the Russian-Ukrainian war, it has become very important to use the renewable energy potential, which is our country's own resources, to the maximum extent. Since Turkey lacks important energy sources such as natural gas and oil, it has to endure a large current account deficit, especially in energy expenses. To meet this increasing demand for electrical energy and to minimize the current account deficit, Turkey has to commission all the renewables. In this context, the development of hydroelectric potential and its presentation for the benefit of the country's economy will be possible by increasing the share of

hydroelectric energy in total energy generation along with other renewable energy sources [8-10].

The annual electricity consumption per capita in Turkey is at the level of 3.300 kWh, and this amount remains below the average electricity energy consumption of European countries. Since industrialization is a goal for ensuring the economic and social development of our country, it is of great importance that the energy needed by this industry and other users is met on the spot, on time and reliably. In this term, if economic recessions are not taken into account, electricity consumption in Turkey increases by 4-10% every year. In order to meet this demand, Turkey has to separate to spend 4 billion US dollars every year for new energy generation projects [6,11,12].

Since to have self-sufficient, continuous, reliable and economic electric power is a vital issue for Turkey as in the entire world, Turkey has to be definitely taken account of hydropower and other renewable energy alternatives which are local, independent and domestic energy sources in the form of being maximum benefit.

In addition, Turkey has to build more dams and hydroelectric power plants than other countries because it is not a country that receives rainfall every season due to its geographical location. Hydroelectric power plants are important due to their advantages such as environmental friendliness, revitalization of the economic and social structure in rural areas, low potential risk and the ability to respond to sudden changes in demand.

This article aims to consider hydropower as a whole and evaluate the data for the year 2021. In this context, first of all, Turkey's 2021 energy data are reviewed, and then hydropower is investigated in detail.

2. ENERGY IN TURKEY : SUMMARY DATA OF 2021

Structural arrangements made in recent years to encourage the use of renewable energy sources instead of imported sources in electricity generation continued to show their results despite the developments experienced during and as a result of the Covid-19 pandemic in the markets. In this context, the share of renewable energy sources, which was 51.4 % in 2020, including unlicensed electricity, increased to 53.34% in 2021. In addition, despite the pandemic conditions, two new products were put into service in Turkey's electricity market in 2021, namely the Forward Electricity Market (VEP) and the Renewable Energy Source Guarantee (YEK-G) System and the Organized YEK-G Market[13, 14].

Turkey is a country where the resources and ability to fully provide its own generated energy. While total installed capacity was 69.516 MW in 2014, this capacity reached 99.819 MW as of 31 December 2021. The installed capacity has increased thanks to the installation of new natural gas, solar power, and hydropower and wind power plants. Within the energy mix, hydropower has become the primary source of energy, accounting for 31.55 % of the installed capacity[13-16].

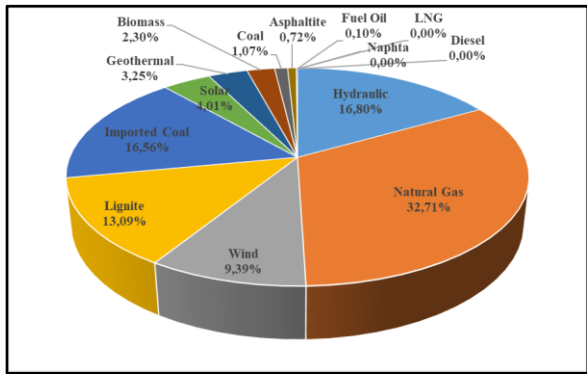
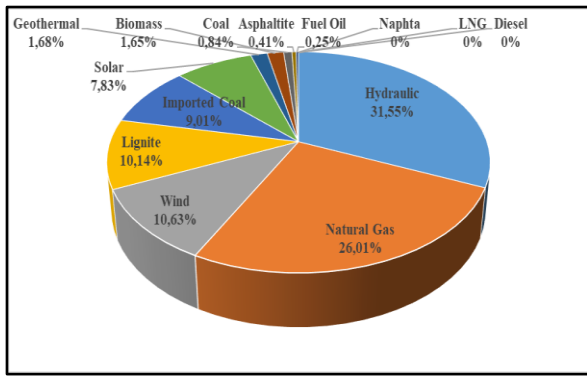
From the other energy sources, 26.01 % can be attributed to gas fired power plants, 19.99 % to coal (coal+lignite), almost 10.63 % to wind, 7.83 % to solar power, 1.68 % to other renewable sources (geothermal and waste heat), 1.66 % to biomass and 0.26 % to other fuels (oil, diesel, naphtha) (Table 1, Figure 1).

In 2021, the actual consumption amount increased by 7.73% compared to 2020 and reached 328,405 GWh. In 2021, electricity imports increased by 23.34% compared to last year and amounted to 2.33 TWh. In 2021, electricity exports increased by 68.56% compared to last year and amounted to 4.19 TWh. The share of renewable energy sources including hydraulics in total installed power increased from 48% by the end of 2020 to 50.02% in 2021. The proportion of total thermal power installed decreased from 52% in 2020 to 49.98% in 2021 [13-16].

The share of hydropower in electricity generation was around 16.80% in 2021, while the share of renewable energy including hydropower remained around 35.75%(Table 1,Figure 1)

Table 1. Breakdown of Installed Capacity and Generation by Sources in 2021 [13]

Fuel/Source Type	Total InstalledCapacity* (MW)	Ratio (%)	Total Generation* (MWh)	Ratio (%)
Hydraulic	31,492.58	31.55	55,695,231.65	16.80
Natural Gas	25,964.56	26.01	108,438,726.84	32.71
Wind	10,606.98	10.63	31,137,427.23	9.39
Lignite	10,119.92	10.14	43,400,430.26	13.09
ImportCoal	8,993.80	9.01	54,888,840.62	16.56
Solar	7,815.63	7.83	13,294,280.97	4.01
Geothermal	1,676.17	1.68	10,770,879.81	3.25
Biomass	1,644.52	1.65	7,616,648.91	2.30
Coal	840.77	0.84	3,539,791.50	1.07
Asphaltite	405.00	0.41	2,372,954.47	0.72
FuelOil	251.93	0.25	336,644.04	0.10
Naphta	4.74	0.00	0.00	0.00
LNG	1.95	0.00	0.00	0.00
Diesel	1.04	0.00	78.33	0.00
Total	99,819.57	100.00	331,491,934.64	100.00



* Licensed and unlicensed power plants are included.

Figure 1. Breakdown of Total Installed Capacity(left) and Generation(right) by Sources in 2021[13]

While the share of natural gas power plants (including liquid and natural gas fired power plants) within the licensed installed capacity was 28.80% at the end of 2020, it decreased to 27.64% in 2021, the share of dam-hydroelectric power plants decreased from 25.74% to 25.23%. The share of river-hydroelectric power plants decreased from 9.04% to 8.88%. Also, while the share of power plants based on import coal decreased from 10.09% to 9.75%, the share of lignite power plants decreased from 11.36 % to 10.97%. In 2021, the licensed installed capacity increased by 3.60% compared to last year and reached 92.272,58 MW. Between 2020 and 2021 the installed capacity has developed on the basis of renewable energy (Table 2, Figure 2). On the other hand, the share of wind power plants, which was 9.80% in licensed installed capacity, increased to 11.42% and the share of geothermal power plants increased from 1.80% to 1.82% in 2021[13-16]

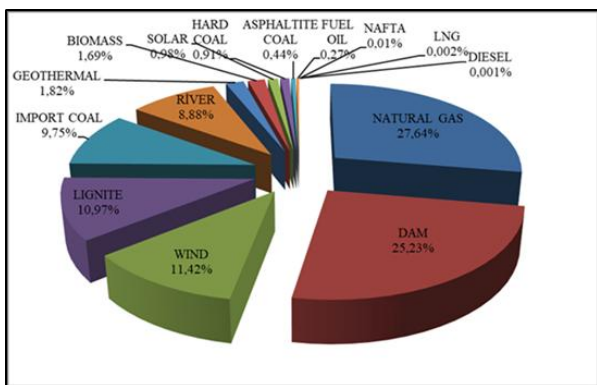


Figure 2. Distribution of Licensed Installed Capacity by Energy Sources in 2021[13]

Table 2. Changes in Licensed Installed Capacity by Sources between 2020 and 2021 [13-16]

Fuel/Source Type	2020 (MW)	Ratio (%)	2021 (MW)	Ratio (%)	Change(%)
Natural Gas	25,639.26	28.80	25,501.51	27.64	-0.54
Hydraulic(Dam)	22,925.03	25.70	23,280.37	25.23	1.55
Wind	8,761.57	9.80	10,533.90	11.42	20.23
Lignite	10,119.92	11.40	10,119.92	10.97	0.00
Import Coal	8,986.85	10.10	8,993.80	9.75	0.08
Hydraulic(River)	8,050.23	9.00	8,198.23	8.88	1.84
Geothermal	1,613.19	1.80	1,676.17	1.82	3.90
Biomass	1,031.88	1.20	1,555.41	1.68	50.74
Solar	409.80	0.50	907.85	0.98	121.53
Coal	810.77	0.90	840.77	0.91	3.70
Asphaltite	405.00	0.50	405.00	0.44	0.00
Fuel Oil	305.93	0.30	251.93	0.27	-17.65
Naphta	4.74	0.00	4.74	0.01	0.00
LNG	1.95	0.00	1.95	0.00	0.00
Diesel	1.04	0.00	1.04	0.00	0.00
Total	89,067.13	100.00	92,272.58	100.00	3.60

The share of renewables such as geothermal, wind, solar and biomass resources in installed capacity has increased every year (Figure 3). The share of EÜAŞ power plants in total installed capacity, 24.05% in 2020, decreased to 23.10%. Also, the share of power plants operating under existing contracts in total installed capacity decreased from 4.21% to 3.33% compared to the previous year. On the other hand, while the share of independent companies operating under free market conditions was 72.62% in 2020, it increased to 73.57% in 2021 (Figure 4).

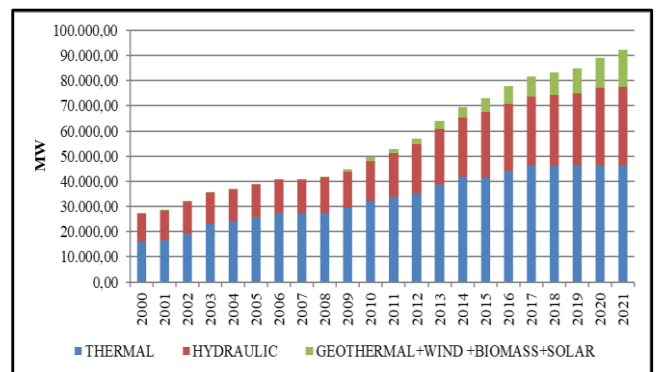


Figure 3. The Development of Licensed Installed Capacity by Source over the Years (MW) [13]

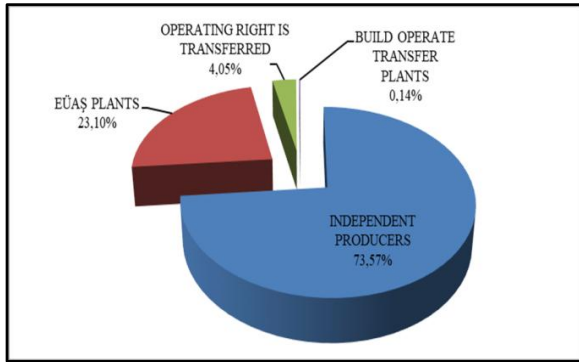


Figure 4. Breakdown of Licensed Installed Capacity by Operators in 2021 [13-16]

The share of licensed electricity generation in 2021 increased by 8.57% compared to 2020 and reached 319.275,22 GWh. While the generation from licensed renewable sources decreased between 2020 and 2021 electricity generation from fossil fuel sources increased (Table 3, Figure 5).

Table 3. Changes in Licensed Electricity Generation by Energy Sources between 2020 and 2021 [13]

Fuel/Source Type	2020 (GWh)	Ratio (%)	2021 (GWh)	Ratio (%)	Change(%)
Natural Gas	69,277.54	23.60	108,394.45	33.95	56.46
Hydraulic	78,087.88	26.60	55,656.34	17.43	-28.73
Importad Coal	62,466.47	21.20	54,888.84	17.19	-12.13
Lignite	38,163.85	13.00	43,400.43	13.59	13.72
Wind	24,561.36	8.40	30,990.13	9.71	26.17
Geothermal	9,929.41	3.40	10,770.88	3.37	8.47
Biomass	5,228.50	1.80	7,371.77	2.31	40.99
Cola	3,415.83	1.20	3,539.79	1.11	3.63
Asphaltite	2,222.88	0.80	2,372.95	0.74	6.75
Solar	416.98	0.10	1,552.91	0.49	272.42
FuelOil	313.04	0.10	336.64	0.11	7.54
Diesel	1.00	0.00	0.08	0.00	-92.17
Total	294,084.73	100.00	319,275.22	100.00	8.57

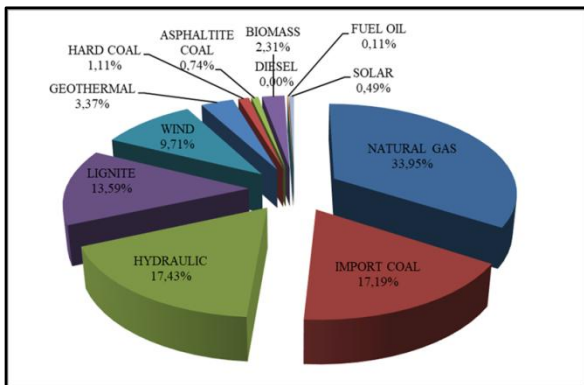


Figure 5. Breakdown of Licensed Electricity Generation by Sources in 2021 [13-16]

In 2021, the unlicensed installed capacity increased by 10.60% compared to the previous year and became 7,546.99 MWe. 91.53% of this amount is based on solar energy. The amount of capacity that entered the facility, which was 6,823.47 MWe at the end of 2020, increased by 10.6%. As in 2020, the highest share belongs to solar power plants with 91.53% in 2021, followed by natural gas with 6.14% and biomass with 1.18% (Table 4, Figure 6).

Table 4. Changes in Unlicensed Installed Capacity by Energy Sources between 2020 and 2021 [13]

Fuel/Source Type	2020		2021		Change (%)
	Installed Capacity (MWe)	Ratio (%)	Installed Capacity (MWe)	Ratio (%)	
Solar	6,257.61	91.71	6,907.78	91.53	10.39
Natural Gas	402.67	5.90	463.05	6.14	14.99
Biomass	83.71	1.23	89,11	1.18	6.45
Wind	70.83	1.04	73.08	0.97	3.17
Hydraulic	8.65	0.13	13.98	0.19	61.64
Total	6,823.47	100.00	7,546.99	100.00	10.60

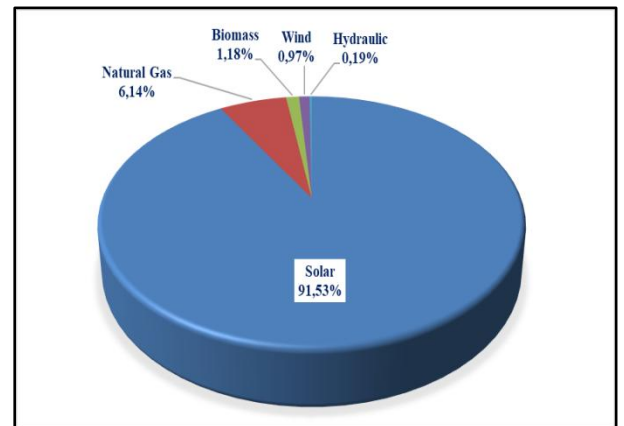


Figure 6. Breakdown of Unlicensed Installed Capacity by Sources in 2021 [13-16]

In 2021, the amount of unlicensed generation increased by 6.27% compared to 2020. While the amount of energy supplied to the grid within the scope of unlicensed electricity generation was 11,245.48 GWh in 2020, it increased by 6.27% to 11,950.26 GWh in 2021. Of this 96.62% was produced from the sun, 2.10% from biomass, and 1.29% from wind and hydraulics. In 2021, the share of hydraulic and solar energy in unlicensed electricity generation increased by 26.03% and 6.66%, respectively, while the share of biomass and wind decreased by 8.26% and 0.44%, respectively (Table 5, Figure 7).

Therefore, it can be predicted that renewable energy generation will take an important place in unlicensed electricity generation in the future.

Table 5.Changes in Unlicensed Electricity Generation by Energy Sources between 2020 and 2021[13]

Fuel/Source Type	2020		2021		Change (%)
	The amount of extra energy supplied to the system (GWh)	Ratio (%)	The amount of extra energy supplied to the system (GWh)	Ratio (%)	
Solar	10,825.50	96.27	11,546.36	96.62	6.66
Biomass	273.45	2.43	250.86	2.10	-8.26
Wind	119.47	1.06	118.94	1.00	-0.44
Hydraulic	2,707	0.24	34.11	0.29	26.03
Total	11,245.48	100.00	11,950.26	100.00	6.27

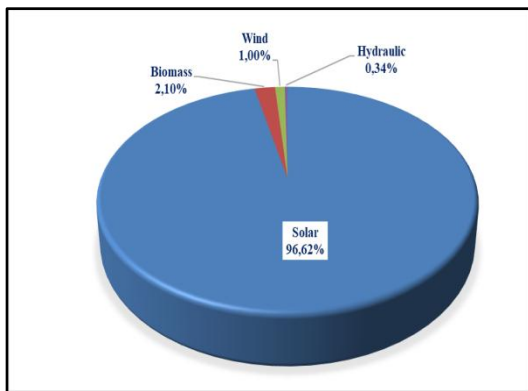


Figure 7. Breakdown of Unlicensed Electricity Generation by Resources in 2021

3. HYDROPOWER POTENTIAL IN TURKEY: DATA OF 2021

The theoretical hydroelectric potential in Turkey is calculated as 433 billion kWh/year, and the technically evaluable potential is calculated as 216 billion kWh/year. The technical hydropower potential of Turkey corresponds to 1.5% of the world's technical hydropower potential and 18% of the European technical hydropower potential. The USA has developed 86% of its technical hydropower potential, Japan 78%, Norway 72%, Canada 56%, and Turkey 50% [12,13].

Turkey's hydraulic potential is 55.000 MW, and the share of hydraulic installed power has reached 31.647 MW from 11.175 MW in 2000 as of 31 December 2021, in total installed power is 32.9 % hydraulic installed capacity will be about 32 GW in 2023 according to MENR's Strategic Plan 2019-2023[17].In cooperation with the public - private sector 743 Hydroelectric Power Plants have completed and commissioned with an installed capacity of 31.647 MW and an energy generation potential of approximately 109 Billion kWh in cooperation with the Public-Private sector as of 31.12.2021(Table 6).

Table 6. Hydropower Potential of Turkey [6]

Potential	Number	Total Installed Capacity (MW)	Generation (GWh/Year)	Ratio (%)
In operation	743	31,647	108,932	68.8
Under construction	26	1,141	4,090	2.6
Project	469	15,143	45,379	28.6
Total	1,238	47,931	158,401	100

From 743 facilities, 68 facilities with an installed capacity of 13,766 MW and an energy generation potential of 49 Billion kWh were established by DSI; 646 facilities with an installed capacity of 17,881 MW and an energy generation potential of 60 Billion kWh have been built and put into operation by the private sector (Table 7).

The construction of those built by the Public from these facilities is carried out by DSI and the operation is transferred to EUAS, while those built by the private sector, except for the EMRA license, are other (water use right agreement, project, construction, acceptance of water structures, etc.) operations are performed by DSI.

Turkey is very rich in hydroelectric, geothermal, solar and wind energy sources and has a very high potential to develop these resources. Accordingly, development of renewable energy sector in Turkey is highly encouraged. At the end of December 2021, share of renewable energy in total installed capacity exceeded 50%.

Electricity demand, which is one of the most important indicators of economic growth, has experienced great fluctuations on a global scale due

to the measures implemented to prevent the Covid-19 pandemic. The effect of the slowdown in economic activity of the measures taken in this context was also seen in the electricity demand as of the end of the year. Turkey has been among the least affected countries by the epidemic with an increase of 7.89 % in electricity demand in December 2021.

The structural arrangements made in recent years to encourage the use of renewable energy sources instead of imported sources in electricity generation have continued to show their results despite the developments experienced and resulting from the Covid-19 pandemic in the markets. In this context, the share of renewable energy sources, which was 51.4% in the total installed electricity capacity in 2020, including unlicensed ones, increased to 53.34% in 2021. In addition, despite the pandemic conditions, two new products put into service in the electricity market of our country in 2021, namely the Term Electricity Market (VEP), the Renewable Energy Resource Guarantee (YEK-G) System and the Organized YEK-G Market [13].

Table 7. Hydroelectric Potential Development of Turkey as of 31 December 2021 [6]

Stage of Project	Operator (Public/Private)	Number	Installed Capacity (MW)	Generation Potential (GWh/year)	Ratio (%)
In Operation	DSI (Public)	68	13,766	48,952	27.2
	Private	675	17,881	59,980	33.3
	Total	743	31,647	108,932	60.5
Under Construction	DSI (Public)	2	700	2,569	1.4
	Private	24	441	1,521	0.9
	Total	26	1,141	4,090	2.3
Inspection and Project	Private	160	5,853	16,799	9.4
	Private (declared in Table)	7	247	778	0.4
	DSI (Prelicense-Planned)	33	1,398	4,122	2.3
	Total	200	7,498	21,699	12.1
Total potential (Operation-construction-inspection-project)		969	40,286	134,721	74.9
Possible projects over 10 MW		269	7,645	23,680	13.2
Potential to be developed by 2023		1,238	47,931	158,401	88.1
SHP projects to be developed		625	2,646	8,728	4.8
Potential to be developed after 2023		--	4,423	12,871	7.1
POTENTIAL GENERAL		1,863	55,000	180,000	100.0

4. CONCLUSION AND RECOMMENDATIONS

Though hydraulic installed capacity will be about 32 GW in 2023 according to Strategic Plan 2019-2023 of Ministry of Energy and Natural Resources, this prediction seems to have come true from today. The share of hydroelectric installed capacity and power generation has increased around 1 % from last year in 2021. However, this increase is insufficient compared to increase in other energy sources.

Especially with the widespread distribution of natural gas in recent years, the use of natural gas in both homes and industry has increased, and “Natural Gas Cycle Power Plants” have been established to meet the increasing energy needs. As a result, the share of energy produced from hydropower has decreased in recent years, and the share of thermal energy generation has increased. The European Union has adopted on supporting green energy (hydropower, wind, solar and biomass) in its energy policies. In this case, the energy policies in force in Turkey and the related it has become mandatory to decouple the differences between the legal legislation and the legislation of the European Union. In this context, it is very important to use the renewable energy potential, which is the natural resources of a country, to the maximum extent, and this should be a state policy. As a result, it is necessary to increase the share of hydroelectric energy in the total energy generation in Turkey by improving the hydroelectric potential and

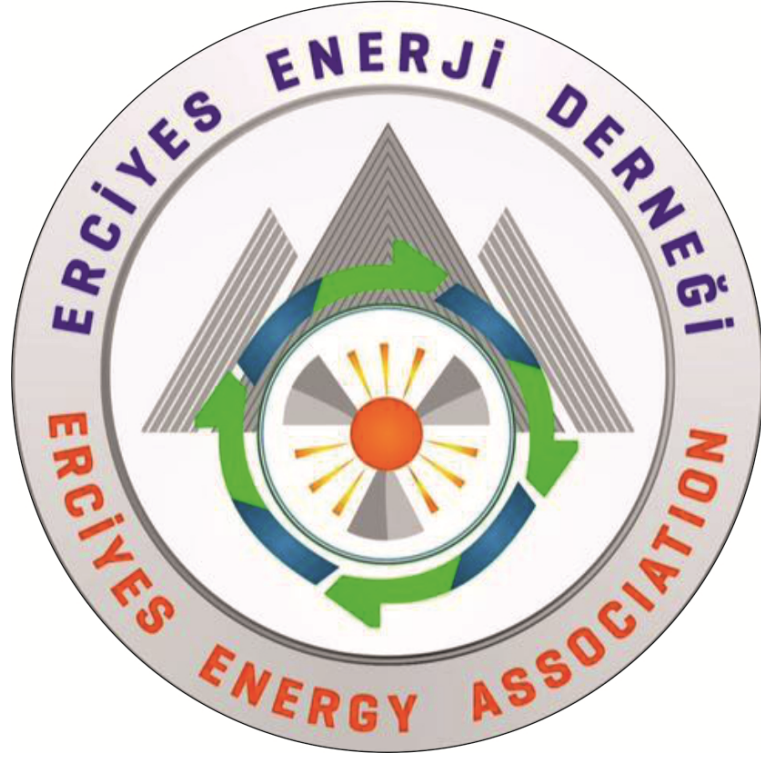
making it available for the benefit of the country's economy.

Turkey consists of 25 hydrological basins, and the water that forms the basis of these basins is a vital and socially important resource. In terms of water resources, the precipitation regime of our country, which is located in a semi-arid region of the world, varies greatly according to the seasons and regions, and it is observed that water needs in some basins have exceeded the potential of resources. Therefore Turkey is vulnerable to climate change and it causes additional stress to water availability in Turkey. This situation may significantly jeopardize the use of both water resources and hydraulic energy in the future. Therefore, in addition to diversifying energy, it is necessary to take the path of benefiting from water resources by providing maximum efficiency. Moreover dam and canal type HEPP projects abandoned by the investor for various reasons should be re-evaluated and their construction should be started after they are made efficient. Some hydro projects should be included in the investment program by DSI considering environmental, social and cultural sensitivities [18] and the hydroelectric energy to be obtained from these facilities should be brought to the economy. On the other hand, the necessary security measures should be taken at the border dams to ensure that the investor companies start working and the facilities should be completed and put into service as soon as possible.

REFERENCES

- [1] Bobat, A. Reasons and results of water shortage in Turkey: The case study of Kocaeli, 2nd EWaS International Conference “Efficient & Sustainable Water Systems Management toward Worth Living Development”, Proceedings, 1-12, 1- 4 June, 2016 - Chania, Crete/Greece, 2016.
- [2] Turkish Ministry of Foreign Affairs. Turkey's Policy on Water Issues, 2021. https://www.mfa.gov.tr/turkey_s-policy-on-water-issues.en.mfa, Accessed on 15 November 2022
- [3] Ozturk M, Bezir NC, Ozek N. Hydropower-water and renewable energy in Turkey: sources and policy, Renewable and Sustainable Energy Reviews 13:605-15, 2009.
- [4] MENR (Ministry of Energy and Natural Resources of Turkey). Elektrik, 2022. <https://enerji.gov.tr/bilgi-merkezi-enerji-elektrik> Accessed on 14 November 2022.
- [5] Edinger R, Kaul S. Humankind's detour toward sustainability: past, present and future of renewable energies and electric power generations, Renewable and Sustainable Energy Reviews 4, 295-313, 2000.
- [6] DSI (State Hydraulic Works), Activity Report-2021, 2022, Ankara. https://cdniys.tarimorman.gov.tr/api/File/GetFile/425/Sayfa/759/1107/DosyaGaleri/2021_yili_faaliyet_raporu.pdf. Accessed on 10 November 2022.
- [7] Bobat, A., Özdemir, N.C. Türkiye'nin Yenilenebilir Enerji Politikaları :Yenilenebilir Enerjide Yeniden Yapılanma, Electronic Journal of Vocational Colleges, 148-158, 2016.

- [8] Binder, J. Small hydroelectric power plants: a most efficient contribution to renewable energy, Karntner Elektrizitäts Aktiengesellschaft (KELAG). Sixty International Summer School Solar Energy. Applications-Sustainable Energy Issues, University of Klagenfurt, Klagenfurt/Carinthia, Austria, 204-214, 2000.
- [9] Kaygusuz K. 2004. Hydropower and world's energy future. *Energy Sources* 26,215-224.
- [10] Yılmaz, A.O. Renewable energy and coal use in Turkey. *Renewable Energy* 33,950-959, 2008.
- [11] Bobat, A. Environmental impact assessment of hydropower projects in Turkey : Applications and problems, *Fresenius Environmental Bulletin*, 26(2), 1192-1200, 2017.
- [12] Bobat, A. Hydroelectric Power Outlook in Turkey, International World Energy Conference, 3 - 04 Aralık 2021, Kayseri-Türkiye, Proceedings Book, 319-325, 2021.
- [13] Energy Market Regulatory Authority (EMRA). Electricity Sector Report-2022, 2022. <https://www.epdk.gov.tr/Detay/Icerik/3-0-23/elektrikaylik-sektor-raporlar>, Accessed on 10 November 2022.
- [14] Ministry of Energy and Natural Resources (MENR). Electricity Sector Report-2022 <https://www.epdk.gov.tr/Detay/Icerik/5-12720/energy-market-regulatory-authority-emra-electri>. Accessed on 9 November 2022.
- [15] TEİAŞ, 2022. 2021 Yılı Elektrik Üretim-Tüketim Raporu. <https://www.teias.gov.tr/aylik-elektrik-uretim-tuketim-raporlari>. Accessed on 5 November 2022.
- [16] The Chamber of Electrical Engineers, Electricity statistics of Turkey, https://www.emo.org.tr/ekler/8c33ba5c2f4fbae_ek.pdf?dergi=1275, Accessed on 7 November 2022.
- [17] MENR. *Strategic Plan 2019-2023*. 2019. http://www.sp.gov.tr/upload/xSPStratejikPlan/files/muqqm+Stratejik_Plan_2019-023.pdf. Accessed on 6 November 2022.
- [18] Bobat, A. Environmental management aspects in hydro projects, 9th Sustainable Energy and Environmental Protection, Kayseri, Türkiye, 22 - 25 Eylül 2016, Proceedings Book, Volume 1, 478-489, 2016.



Founded in 2016, our association is open to everyone who is interested in energy and devoted to sustainability.

ERCIYES ENERGY ASSOCIATION

2022